

FACULTY
OF MATHEMATICS
AND PHYSICS
Charles University

1

BACHELOR THESIS

2

Martin Vavřík

3

**Simulation and Reconstruction
of Charged Particle Trajectories
in an Atypic Time Projection Chamber**

4

5

Institute of Particle and Nuclear Physics

6

Supervisor of the bachelor thesis: Mgr. Tomáš Sýkora, Ph.D.

7

Study programme: Physics

8

Prague 2025

- ⁹ I declare that I carried out this bachelor thesis independently, and only with the
¹⁰ cited sources, literature and other professional sources. It has not been used to
¹¹ obtain another or the same degree.
- ¹² I understand that my work relates to the rights and obligations under the Act
¹³ No. 121/2000 Sb., the Copyright Act, as amended, in particular the fact that the
¹⁴ Charles University has the right to conclude a license agreement on the use of this
¹⁵ work as a school work pursuant to Section 60 subsection 1 of the Copyright Act.

In date
Author's signature

¹⁶ Dedication.

Title: Simulation and Reconstruction of Charged Particle Trajectories in an Atypical Time Projection Chamber **Added hyphen to avoid overfull hbox**

Author: Martin Vavřík

Institute: Institute of Particle and Nuclear Physics

Supervisor: Mgr. Tomáš Sýkora, Ph.D., Institute of Particle and Nuclear Physics

Abstract: Abstract.

Keywords: key words

¹⁷ Contents

¹⁸	Motivation	³
¹⁹	0.1 ATOMKI Anomaly	³
²⁰	0.1.1 ATOMKI Measurements	³
²¹	0.1.2 Other Experiments	⁴
²²	0.2 X17 Project at IEAP CTU	⁶
²³	1 Time Projection Chamber	⁹
²⁴	1.1 Charge transport in gases	⁹
²⁵	1.1.1 Drift	⁹
²⁶	1.1.2 Diffusion	¹¹
²⁷	1.2 Readout	¹²
²⁸	1.2.1 Multi-Wire Proportional Chamber	¹²
²⁹	1.2.2 Gas Electron Multiplier	¹²
³⁰	1.2.3 Micromegas	¹²
³¹	1.2.4 Parallel Plate Chamber	¹³
³²	1.3 Orthogonal Fields TPC at IEAP CTU	¹³
³³	1.3.1 Motivation and Associated Challenges	¹³
³⁴	1.3.2 Coordinate Systems and Dimensions	¹⁴
³⁵	1.3.3 Magnetic Field Simulation	¹⁶
³⁶	2 Track Simulation	¹⁹
³⁷	2.1 Microscopic Simulation	¹⁹
³⁸	2.1.1 First testing track	²⁰
³⁹	2.1.2 Grid-like testing sample	²⁰
⁴⁰	2.2 Runge-Kutta Simulation	²⁰
⁴¹	2.2.1 Testing sample	²³
⁴²	3 Track Reconstruction	²⁵
⁴³	3.1 Reconstruction Assuming Steady Drift	²⁵
⁴⁴	3.2 Ionization Electron Map	²⁷
⁴⁵	3.2.1 Gradient Descent Algorithm	³⁰
⁴⁶	3.2.2 Interpolation on the Inverse Grid	³¹
⁴⁷	3.3 Discrete Reconstruction	³³
⁴⁸	4 Energy Reconstruction	³⁵
⁴⁹	4.1 Cubic Spline Fit	³⁵
⁵⁰	4.2 Circle and Lines Fit	³⁷
⁵¹	4.2.1 Two-dimensional fit	³⁸
⁵²	4.2.2 Three-dimensional fit	³⁹
⁵³	4.2.3 Testing on a Runge-Kutta sample	⁴¹
⁵⁴	4.3 Runge-Kutta Fit	⁴²
⁵⁵	4.3.1 Testing on a microscopic sample	⁴⁴
⁵⁶	Conclusion	⁴⁶
⁵⁷	Bibliography	⁴⁹

Motivation

59 A Time Projection Chamber (TPC) [refs] is a type of gaseous detector that detects
60 charged particle trajectories by measuring the positions and drift time of ions cre-
61 ated in the gas. The energies of these particles can be inferred from the curvatures
62 of their trajectories in the magnetic field (**specific field inside the TPC**).

63 The goal of this thesis is to develop an algorithm for the reconstruction of
64 charged particle trajectories and energy in an *atypic* TPC with orthogonal elec-
65 tric and magnetic fields, hereafter referred to as the Orthogonal Fields TPC
66 (OFTPC), used in the X17 project at the Institute of Experimental and Applied
67 Physics, Czech Technical University in Prague (IEAP CTU). Furthermore, we
68 present the results of testing of several (gradually improving) developed algo-
69 rithms with different samples of simulated data. **Put this somewhere, (maybe
70 just the abstract?). We use the Garfield++ toolkit [1] for simulations in combina-
71 tion with the ROOT framework [2] for data analysis and visualization. Some of
72 our more demanding simulations are run on the MetaCentrum grid [3].**

73 The X17 project in IEAP CTU aims to reproduce measurements of anomalous
74 behavior in the angular correlation distribution of pairs produced by the Internal
75 Pair Creation (IPC) mechanism [4] during the decay of certain excited nuclei
76 (⁸Be, ¹²C, and ⁴He) observed by a team at ATOMKI in Hungary. **I would leave
77 this here as a short summary before I explain it in more detail in the sections
78 below.**

79 Add citations: X17 project, VdG. Maybe also TPC, etc.

80 0.1 ATOMKI Anomaly

81 Many different theories propose the existence of *new light boson(s)* that are weakly
82 coupled to ordinary matter [5]. These particles are potential dark matter candi-
83 dates and could contribute to a solution of other issues with the Standard Model,
84 such as the strong CP problem and the anomalous muon magnetic moment. **Mass
85 range of axions?**

86 A possible way of detecting such bosons with a short lifetime is to observe
87 nuclear transitions of excited nuclei. If a boson was emitted during the transition
88 and subsequently decayed into an electron-positron pair, we could observe this as
89 a peak on top of the standard e^+e^- (**both cursive and upright forms are used in
90 different articles**) angular correlation from the Internal Pair Creation (IPC) and
91 the External Pair Creation (EPC).

92 0.1.1 ATOMKI Measurements

93 Historically, there were several measurements of the IPC in nuclear transitions
94 in ⁸Be at Institute für Kernphysik (Frankfurt) [6, 7, 8] and at ATOMKI (De-
95 brecen, Hungary) [9, 10] resulting in different anomalies with invariant mass in
96 the range 5 – 15 MeV. This prompted a development of a better spectrometer at
97 ATOMKI.

98 In 2015, a group at ATOMKI observed an anomalous IPC in ⁸Be [11]. They
99 used the ${}^7\text{Li}(p, \gamma){}^8\text{Be}$ reaction at the $E_p = 1030$ keV proton capture resonance

to prepare the 18.15 MeV excited state ($J^\pi = 1^+$, $T = 0$). This state decays predominantly through M1 transitions to the ground state ($J^\pi = 0^+$, $T = 0$) and to the 3.03 MeV state ($J^\pi = 2^+$, $T = 0$) [12]. **Transition figure – all transitions of isotopes? IPC figure?**

The angular correlation of the e^+e^- pairs created internally in these transitions were measured and compared to the simulation; results from a narrow $E_{\text{sum}} = 18$ MeV region are shown in Figure 0.1a. The simulation includes boson decay pairs for different boson masses. The disparity parameter y is defined as

$$y = \frac{E_{e^-} - E_{e^+}}{E_{e^-} + E_{e^+}}, \quad (0.1)$$

where E_{e^-} and E_{e^+} are the kinetic energies of the electron and positron.

Their experimental setup was later upgraded ([details?](#)) and used for new measurements. In 2022 the ${}^8\text{Be}$ anomaly was also measured using the $E_p = 441$ keV resonance to produce the 17.64 MeV excited state ($J^\pi = 1^+$, $T = 1$) which again decays primarily to the ground state and the 3.03 MeV state [12]. The anomaly was also measured for $E_p = 650$ and 800 keV where E1 transitions from the direct proton capture dominate [13]. The results for e^+e^- with $E_{\text{sum}} \in [13.5, 20]$ MeV are shown in Figure 0.1b.

The newer setup was also used in 2021 to study the ${}^3\text{H}(p, e^+e^-){}^4\text{He}$ reaction at $E_p = 510, 610$ and 900 keV [14], inducing direct and resonant capture populating the overlapping first 20.21 MeV ($J^\pi = 0^+$) and second 21.01 MeV ($J^\pi = 0^-$) excited states [15]. The comparison of simulated and measured e^+e^- pair angular correlations in the $E_{\text{sum}} \in [18, 22]$ MeV region is shown in Figure 0.1c.

In 2022, another anomaly was measured in the ${}^{11}\text{B}(p, e^+e^-){}^{12}\text{C}$ process [16]. The $E_p = 1388$ keV resonance was used to populate the 17.23 MeV excited state ($J^\pi = 1^-$, $T = 1$) with a large width $\Gamma = 1.15$ MeV [17]. This state decays mainly through E1 transitions to the ground state $J^\pi = 0^+$ and to the 4.44 MeV state $J^\pi = 2^+$. To compensate for energy losses in the target, five energies in the range $E_p = 1.5\text{--}2.5$ MeV were used. The experimental angular correlation for the 17.23 MeV transition to the ground state is shown in Figure 0.1d.

Possible explanations of the anomaly include experimental effects, higher order processes in the Standard Model [18, 19] or even a protophobic fifth force mediated by a new 17 MeV boson X17 [20]. **Not sure if the introduction should be referenced since even though it is related, it is an independent theory developed only (?) to explain these measurements. Zhang and Miller: <https://www.sciencedirect.com/science/article/pii/S0370269321000010>**

0.1.2 Other Experiments

Since the ATOMKI measurements, several experiments have been initiated to attempt to replicate the results and search for the hypothetical X17 particle. The following experiments have already produced results. **Could cite the ATOMKI review paper here.**

Two-arm e^+e^- spectrometer in Hanoi

The anomaly in ${}^8\text{Be}$ has been observed with a high ($> 4\sigma$ **That's all they write in their article.**) confidence by a team at the Hanoi University of Sciences for

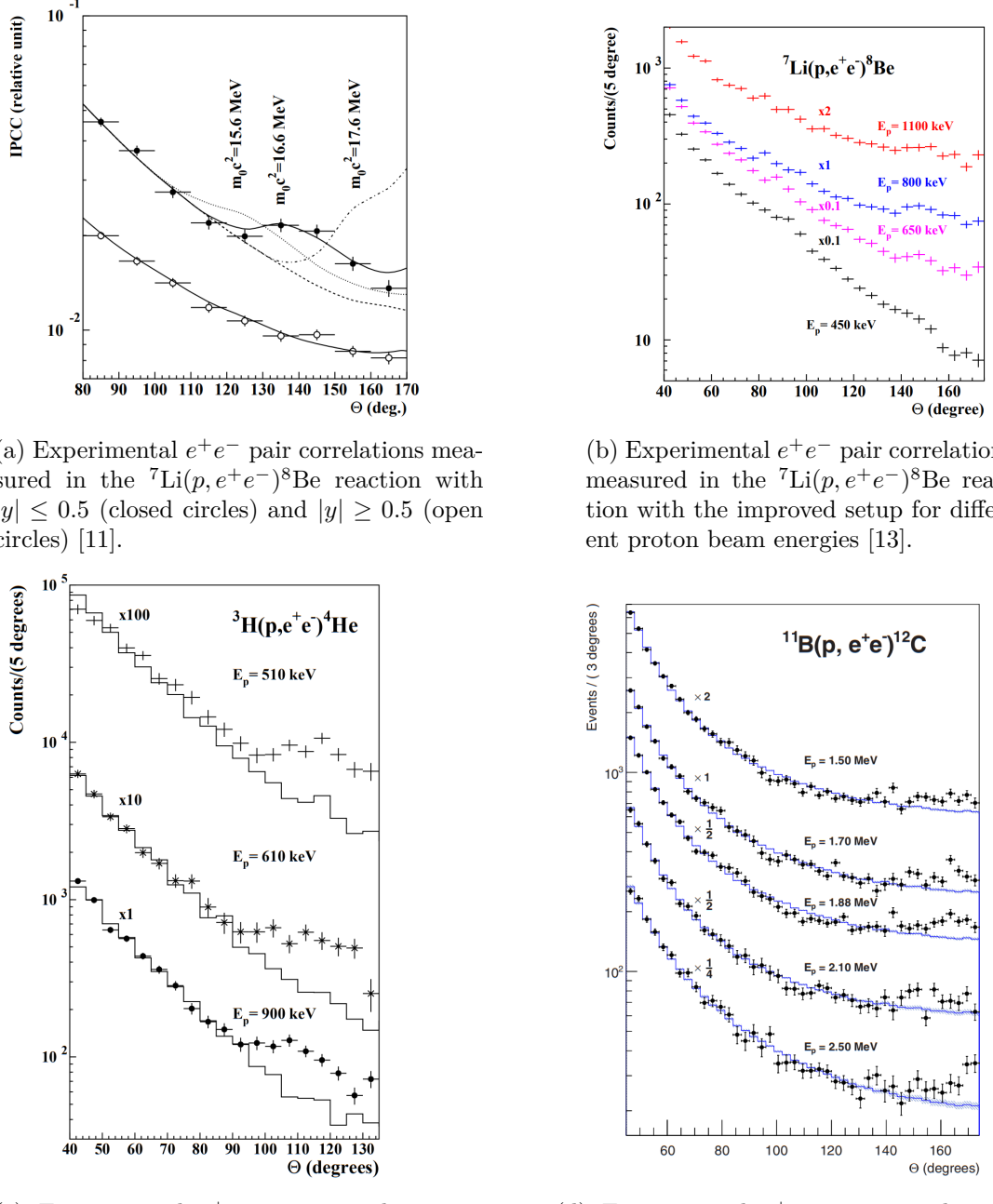


Figure 0.1: The ATOMKI anomalous IPC measured for different nuclei.



Figure 0.2: Results from the Hanoi spectrometer – angular e^+e^- pair correlations measured in the ${}^7\text{Li}(p, e^+e^-){}^8\text{Be}$ reaction at $E_p = 1225$ keV [21].

¹⁴³ $E_p = 1225$ keV [21]. They built a two-arm spectrometer in collaboration with
¹⁴⁴ ATOMKI and calibrated it using the 17.6 MeV M1 transition. The results are
¹⁴⁵ shown in Figure 0.2.

¹⁴⁶ Collisions at Nuclotron in Dubna

¹⁴⁷ At the Joint Institute for Nuclear Research in Dubna, signal in the form of en-
¹⁴⁸ hanced structures in the $\gamma\gamma$ spectra at ~ 17 and 38 MeV invariant masses for
¹⁴⁹ $p + \text{C}$, $d + \text{C}$ and $d + \text{Cu}$ reactions at momenta 5.5 , 2.75 , and 3.83 GeV per nu-
¹⁵⁰ cleon [22]. Monte Carlo simulations support the conclusion that the signals are
¹⁵¹ a consequence of a decay of unknown particles X17 and E38.

¹⁵² The MEG II (Muon Electron Gamma) experiment

¹⁵³ Experiments using the ${}^7\text{Li}(p, e^+e^-){}^8\text{Be}$ reaction were carried out at the Paul
¹⁵⁴ Scherrer Institute with the MEG II superconducting solenoid spectrometer [23].
¹⁵⁵ Analysis of the data with $E_p = 1080$ keV exciting both of the resonances (beam
¹⁵⁶ fully stopping in the target) found no significant evidence supporting the X17
¹⁵⁷ hypothesis, results are shown in Figure 0.3. An upper bound (at 90% confidence)
¹⁵⁸ on the X17-to- γ branching ratio was set at $1.2 \cdot 10^{-5}$ for the 18.15 MeV state
¹⁵⁹ (larger than the ratio $5.8 \cdot 10^{-6}$ obtained by ATOMKI in 2016). Could add their
¹⁶⁰ 90% C.L bounds figure also. Insufficient statistics – 6.2 % (1.5σ) p-value.

¹⁶¹ 0.2 X17 Project at IEAP CTU

¹⁶² The aim of the X17 project at the Van der Graaff facility of the Institute of
¹⁶³ Experimental and Applied Physics, Czech Technical University in Prague is to
¹⁶⁴ repeat the original ATOMKI experiments with ${}^7\text{Li}$ and ${}^3\text{H}$ targets using an inde-
¹⁶⁵ pendent e^+e^- spectrometer. In order to effectively measure the anomaly, we need
¹⁶⁶ to reconstruct both the energy and the angular correlation of the e^+e^- pairs. The

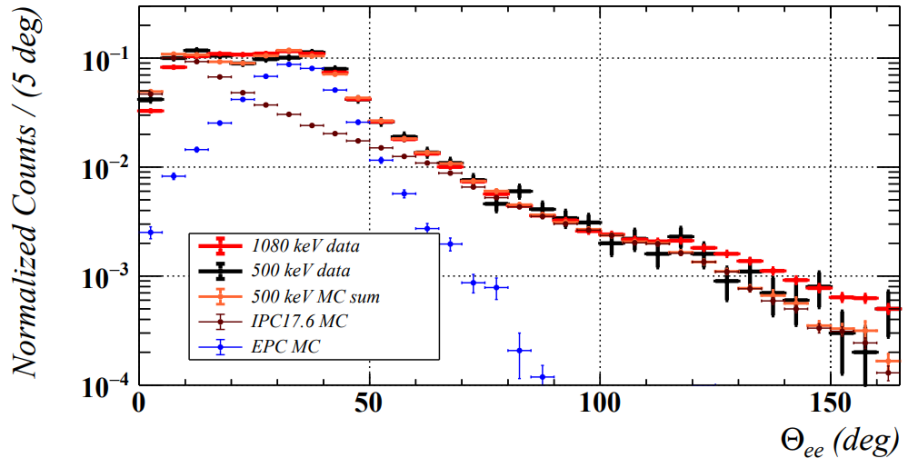


Figure 0.3: Results from the MEG II experiments – angular correlation of e^+e^- pairs with $E_{\text{sum}} \in [16, 20]$ MeV measured in the ${}^7\text{Li}(p, e^+e^-){}^8\text{Be}$ reaction with proton beam energies 500 and 1080 keV. The 500 keV dataset is fitted with Monte Carlo of both the IPC deexcitation and the EPC produced by gammas [23].

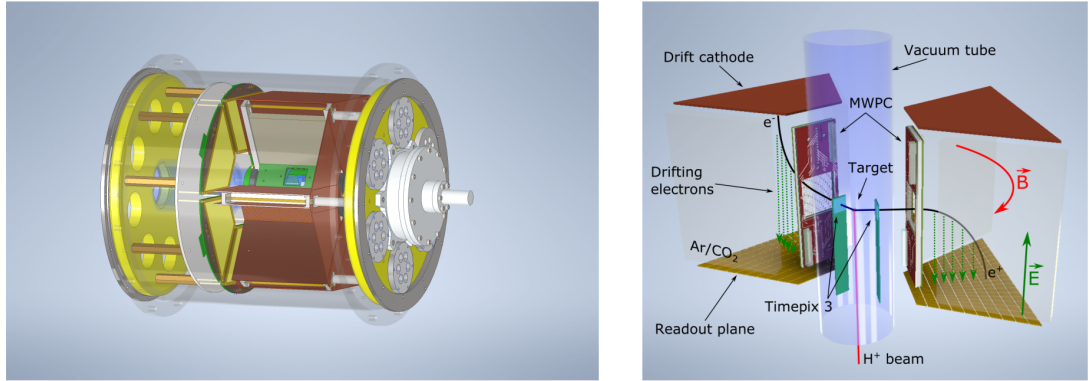


Figure 0.4: Schematics of the detector at the Van der Graaff facility at IEAP CTU.

167 spectrometer will use three layers of detectors to achieve this – Timepix 3 (TPX3)
 168 silicon pixel detector and Multi-Wire Proportional Chamber (MWPC) layers for
 169 the angle reconstruction and a Time Projection Chamber (TPC) layer for the en-
 170 ergy reconstruction. The schematics of the prepared detector is in Figure 0.4
 171 [Spectrometer CAD drawing \(coordinates here or next chapter?\)](#). Cite some VdG
 172 paper, mention grant? Using [https://cernbox.cern.ch/pdf-viewer/public/
 173 rf0oU1nqVLN3acZ/LuzH_submitted.pdf](https://cernbox.cern.ch/pdf-viewer/public/rf0oU1nqVLN3acZ/LuzH_submitted.pdf).

174 The energy of e^+e^- pair produced in the reaction is given by the energy
 175 available E_r in the reaction and can be distributed between them arbitrarily.
 176 Nonetheless in the decay of the hypothetical X17 particle, electron and positron
 177 should have similar energy and we can therefore use a disparity cut $|y| \leq 0.5$
 178 for the disparity parameter (defined in Equation 0.1). Interesting events should
 179 rarely have a particle with an energy below $E_r/4$ (roughly 4 MeV). Electrons with
 180 such low energies are scattered significantly by even a thin layer of relatively light
 181 material, for this reason the TPX3 layer will be inside of the vacuum tube and

182 the tube will have a thinned aluminum segment or KaptonTM windows.

183 TPX3 can measure (in each $55 \times 55 \mu\text{m}$ pixel of its 256×256 grid) time-of-arrival
184 (ToA) with 1.6 ns precision and time-over-threshold (ToT) which reflects the de-
185 posited energy. This potentially allows 3D tracking if we increase the chip thick-
186 ness at the cost of increased scattering. The layer can reconstruct the reaction
187 vertex and the angular correlation with high precision.

188 The layer of MWPCs with sensitive area $40 \times 38 \text{ mm}^2$ will be outside of
189 the beam pipe. It will provide an extra point on the particle trajectory which can
190 help with the estimation of the reaction vertex and improve the TPC performance
191 by providing its entry point.

192 The TPCs, which are a subject of this theses, are in a magnetic field of per-
193 manent magnets positioned between them and provide 3D track reconstruction
194 and subsequent momentum and particle identification (its charge, or even type
195 based on its stopping power). They avoid radiative losses thanks to the small
196 interaction with the incident particle. For the readout, triple Gas Electron Mul-
197 tiplier (GEM) will be used. The magnetic field layout in our TPCs is atypical –
198 orthogonal to the electric field inside the chamber, this is why we call them Or-
199 thogonal Fields TPC (OFTPC). Further details about our OFTPCs are provided
200 in section 1.3.

1. Time Projection Chamber

Using (2010 – a little old) <https://cds.cern.ch/record/1302071/files/CERN-PH-EP-2010-047.pdf>

A Time Projection Chamber (TPC) is a type of gaseous detector that uses the drift in an electric field of free charges (electrons and cations, also anions if attachment of electrons to the gas particles is considered) produced by an ionizing particle to reconstruct its 3D trajectory. When placed inside a magnetic field, the momentum of the incident particle can be inferred from the curvature of its trajectory. Particle identification is also possible using the ionization energy loss inside the TPC (see Figure 1.1). The detector used 80:20 Ar:CH₄ mixture at 8.5 atm pressure.

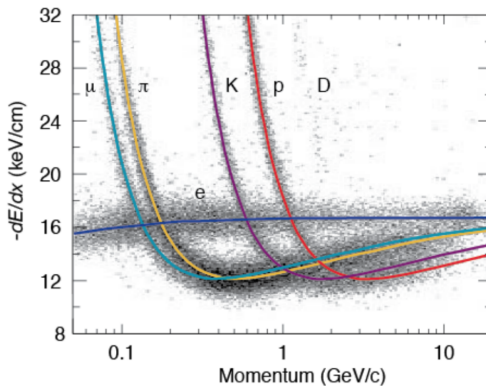


Figure 1.1: Particle identification in the PEP-4 TPC at SLAC based on the energy loss per distance $\frac{dE}{dx}$ [24].

The original TPC used in the PEP-4 experiment at SLAC (Figure 1.2) was a 2×2 m cylinder with a central cathode that produced a strong electric field, making the ionization electrons drift towards one of the bases. The readout consisted of MWPCs, where electrons are accelerated towards the anode wires enough to further ionize the gas and cause an avalanche.

When a charged particle crosses the volume of a TPC, it loses energy by excitation and ionization of the detector gas (how much – from dE/dx + density → footnote?). Most ionizing collision produce a single ionization electron, sometimes a few secondary electrons are produced close to the collision vertex. In rare cases, the ionization electron has energy large enough to create a measurable track, such an electron is called a δ -electron (terminology, just like below – technically it's a (primary) ionization electron causing other (secondary) ionization). Penning transfer (collisions, light – factor 10 for gas gain in Ar/CO₂ viz PDG CERN)?

CERES/NA45 – very inhomogeneous magnetic field

1.1 Charge transport in gases

1.1.1 Drift

Produced ionization electrons (terminology – called ionization electrons in the rest of the thesis, ionoelectrons?) are accelerated towards the readout by the electric

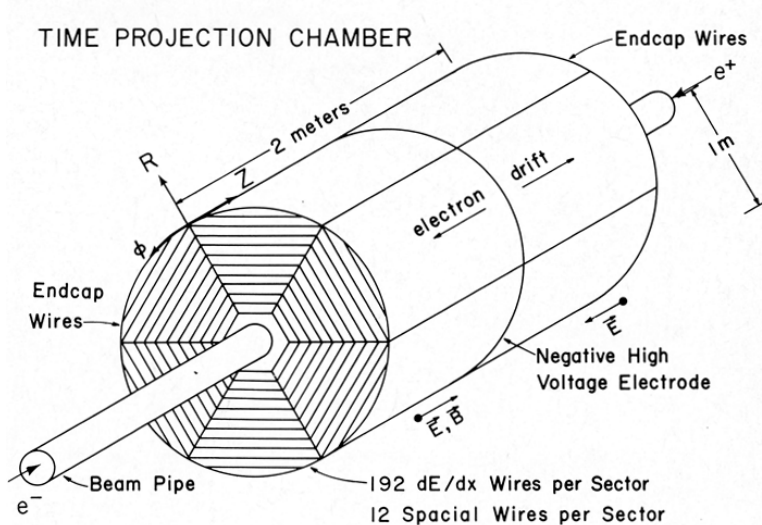


Figure 1.2: Schematic view of the PEP-4 TPC [25]. A charged particle produced in a collision in the beam pipe creates a spiral ionization track in the magnetic field. The central cathode then accelerates ionization electrons towards the endcap anode wires where they are multiplied and read out.

230 field inside the chamber. At the same time, they lose speed by colliding with
 231 the gas particles, quickly reaching a constant (for a given field \mathbf{E}, \mathbf{B}) mean drift
 232 velocity. The electrons might be absorbed by electronegative impurities, such as
 233 halides and oxygen.

234 In many gases (called "hot", e.g., Ar or CH_4), the drift velocity (def? the
 235 paragraph above not enough?) is much greater than that of their thermal motion
 236 thanks to a high proportion of elastic collisions. On the other hand, "cold"
 237 gases like CO_2 have a higher proportion of inelastic collisions (e.g., thanks to
 238 the excitation of rotational and vibrational states) and therefore much lower
 239 (value? magnitude (implied)?) drift velocity.

240 The ions produced by the ionization lose a significant portion of their energy
 241 during each collision since their mass is close to the mass of the gas particles (see
 242 the source material – average energy loss during collision $\Delta E = \frac{2m_i M}{(m_i + M)^2}$, this way
 243 it's more accurate). This, together with their large collision cross section, makes
 244 their drift velocity much smaller and their energy is close to thermal. Since their
 245 momenta aren't randomized to such an extent during collisions, their diffusion
 246 is smaller (more in the sense of distribution of positions, could move this to the
 247 diffusion subsection).

248 The drift is also influenced by the magnetic field. Langevin derived a good
 249 approximation for the drift velocity vector:

$$\mathbf{v}_d = \left(\frac{\mathbf{E}}{\|\mathbf{E}\|} + \omega\tau \frac{\mathbf{E} \times \mathbf{B}}{\|\mathbf{E}\| \|\mathbf{B}\|} + \omega^2\tau^2 \frac{\mathbf{E} \cdot \mathbf{B}}{\|\mathbf{E}\| \|\mathbf{B}\|} \cdot \frac{\mathbf{B}}{\|\mathbf{B}\|} \right) \frac{q\tau}{m(1 + \omega^2\tau^2)} \|\mathbf{E}\|, \quad (1.1)$$

250 where q is the charge of the particle, m is its mass, τ is the mean time between col-
 251 lisions and $\omega = \frac{q}{m} \|\mathbf{B}\|$ is the Larmor frequency. In a standard TPC, \mathbf{E} is nearly
 252 parallel to \mathbf{B} and the influence of the magnetic field on the drift is minimal.
 253 The drift of ions is only negligibly influenced by the magnetic field ($\omega\tau \sim 10^{-4}$ is

254 small due to the low drift velocity – better because it takes τ into account and
255 differs only by E/B ratio). Lorentz angle for orthogonal fields $\tan \psi = -\omega\tau$ (de-
256 viation from electric field) – mention in the OFTPC section. Without magnetic
257 field, we can write

$$\mathbf{v}_d = \frac{q\tau}{m} \mathbf{E} = \mu \mathbf{E}, \quad (1.2)$$

258 where μ is called charge mobility.

259 1.1.2 Diffusion

260 Due to collisions a cloud of electrons or ions originating from the same point will
261 show a Gaussian density distribution at time t while drifting in the electric field
262 $\mathbf{E} = (0, 0, E_z)$ along the z -coordinate (coordinates defined by the electric field):

$$\rho(x, y, z, t) = (4\pi Dt)^{-\frac{3}{2}} \exp\left(-\frac{x^2 + y^2 + (z - v_d t)^2}{4Dt}\right), \quad (1.3)$$

263 where the diffusion coefficient D can be expressed as

$$D = \frac{\lambda^2}{3\tau} = \frac{\lambda v_d}{3} = \frac{v_d^2 \tau}{3} = \frac{2\varepsilon\tau}{3m}, \quad (1.4)$$

264 where λ is the mean free path and ε the mean energy. The lateral diffusion width
265 σ_x after a drift distance L can be expressed as

$$\sigma_x^2 = 2Dt = \frac{4\varepsilon L}{3qE}. \quad (1.5)$$

266 The minimal diffusion width is given by the lowest possible energy of the particles
267 $\varepsilon_{\text{th}} = \frac{3}{2}kT$ (corresponding to thermal motion):

$$\sigma_{x, \text{min}}^2 = \frac{2kTL}{qE}. \quad (1.6)$$

268 For electrons in "cold gases" (e.g., Ar/CO₂ mixture), the diffusion approaches
269 this limit up to a certain field intensity (~ 100 V/cm at 1 atm pressure)¹. In
270 reality, the transversal diffusion of electrons can differ significantly from their
271 longitudinal diffusion and simulations are necessary to get a precise result.

272 In most TPCs, the transversal (but not the longitudinal) diffusion is reduced
273 by the magnetic field, since it is parallel to the electric field and curves the dif-
274 fusing electrons around their mean trajectory:

$$\frac{D_T(B)}{D_T(0)} = \frac{1}{C + \omega^2 \tau_2^2}, \quad (1.7)$$

275 where C and τ_2 are parameters dependent on the gas used. At low intensity of
276 the magnetic field, we can use an approximation $C \approx 1$ and $\tau_2 \approx \tau$.

¹For us $\sigma_{x, \text{min}} = 0.45$ mm, quite close to the actual diffusion 0.5–0.7 mm – details of the calculation.

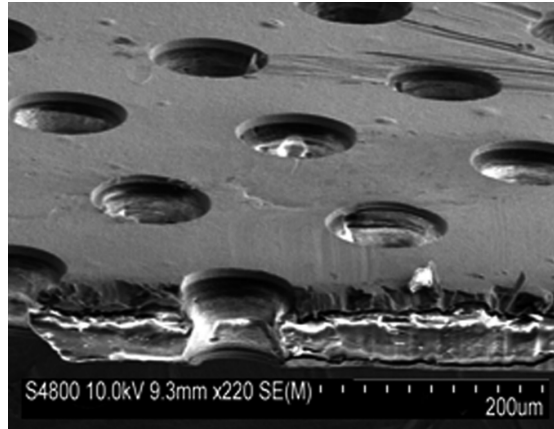


Figure 1.3: A scanning electron microscope image of a GEM foil [26].

277 1.2 Readout

278 1.2.1 Multi-Wire Proportional Chamber

279 In most (2010 – almost all) TPCs operated in experiments Multi-Wire Proportional Chamber (MWPC) (actually wire chamber – similar) was used for the readout. The electrons enter the chamber through a cathode grid and get accelerated 280 in the strong electric field towards the thin anode wires and create a Townsend 281 avalanche (ref), multiplying the signal. Alternating with field wires? That is the 282 difference between MWPC and a drift chamber? The trajectory can be recon- 283 structed using signal from each separate wire. Segmented cathode is also often 284 used for the readout of produced cations. Gating grid (reduction of space charge 285 effect, blocking backflow of ions?, closed for electrons $B=0$, ΔV , static mode (loss 286 of 25% el.) x opening on trigger)? (gas amplification > 10000 required for good 287 SNR, 100-200 ns shaping time), figure – field (acts as a plane from far away and 288 the field only gets strong enough for avalanches)?

291 1.2.2 Gas Electron Multiplier

292 A Gas Electron Multiplier (GEM) is a thin metal-coated polymer sheet with 293 a high density of small holes (Figure 1.3). The amplification is achieved by ap- 294 plying voltage on the metal layers, creating a strong electric field inside the holes 295 and causing avalanches (see Figure 1.4). Double or triple stack of GEMs is usu- 296 ally used to create a sufficient gain. From the last foil, the electrons drift to 297 a segmented anode where the signal is read. The backflow of cations is reduced 298 compared to MWPC. Typical parameters (vs thick GEM?).

299 1.2.3 Micromegas

300 In a MICRO-MEsh GAseous Structure (Micromegas) (in sources I viewed it is not 301 capitalized) electrons pass through a fine mesh (made out of very thin wires) into 302 the narrow amplification gap where they are multiplied in the high field and read 303 as signal on the segmented anode. Very high field ($30-80 \text{ kV/cm}^2$) is necessary 304 to achieve sufficient gain. Cation backflow is heavily suppressed by the mesh.

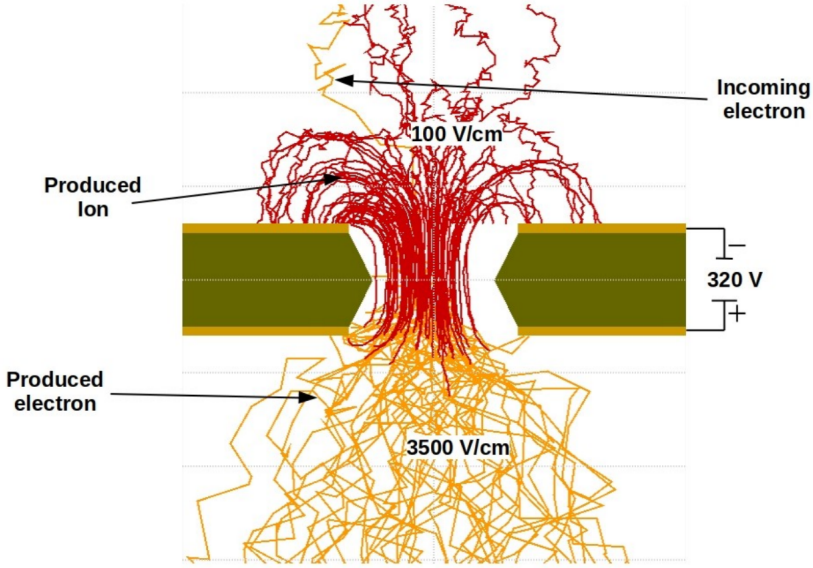


Figure 1.4: Garfield simulation of an avalanche in a GEM hole [27]. An incoming electron (orange) is accelerated in the strong electric field of the GEM and causes further ionization multiplying the number of free electrons (orange). Most of the produced cations (red) are captured by the GEM cathode.

305 1.2.4 Parallel Plate Chamber

306 ... micowell? – these readouts and Micromegas are not used in our detector,
 307 so maybe just mention them at the beginning of the readout section without
 308 excessive detail (some subfigures showing how they look without describing each
 309 too much)

310 1.3 Orthogonal Fields TPC at IEAP CTU

311 At IEAP CTU, we are going to use six identical atypical TPCs with inhomogeneous
 312 toroidal magnetic field **orthogonal** to the electric field ([details below](#)),
 313 hereafter referred to as Orthogonal Fields TPC (OFTPC). It has the shape of
 314 isosceles trapezoidal prism 16 centimeters high with triple-GEM readout on one
 315 of its bases. Dimensions of the OFTPC are discussed in detail in section 1.3.2
 316 below. Throughout this thesis, we assume a uniform electric field along the z axis
 317 with $E_z = -400$ V/cm. [Isn't the field affected by the MWPCs?](#) Measured parti-
 318 cles enter the OFTPC through a window after crossing the MWPC. [Gas mixture](#)
 319 [used in the detector \(70/30\)](#) and its effect – some graph with the mixture. Add
 320 a figure of the real TPC.

321 1.3.1 Motivation and Associated Challenges

322 The reasons for the unusual field layout are mostly cost related:
 323 a) we use permanent magnets instead of a solenoid and parallel fields are
 324 difficult to accomplish this way,
 325 b) granularity of the TPC readout is limited in order to fit one SAMPA/SRS
 326 hybrid in each sector – parallel fields would bend the trajectories parallel

327 to the readout requiring more pads and different architecture.
 328 In this thesis, we will show that such a setup can reach a similar energy resolution
 329 as common cylindrical TPCs while reducing the overall cost.

330 The layout introduces two complications to the track reconstruction – the
 331 trajectory in inhomogeneous field is not circular and the drift is distorted by the
 332 magnetic field as shown in the Equation 1.1(in our case $\omega\tau \approx 0.08$ for 0.3 T
 333 assuming $\mu \approx 0.25 \text{ T}^{-1}$, varies inside the detector). We will deal with these
 334 effects in the upcoming chapters.

335 The diffusion in such setup is larger since parallel orientation reduces diffu-
 336 sion by curling the electrons in the x - y direction (see Equation 1.7), but for our
 337 relatively weak magnetic field and short drift distance, the difference is negligible.

338 1.3.2 Coordinate Systems and Dimensions

339 In order to describe events in our detector, we use three distinct spaces: the de-
 340 tector space \mathcal{D} , the readout space \mathcal{R} and the pad space \mathcal{P} (**different spaces that**
 341 **describe different things and each has their own coordinate system, so maybe**
 342 **rename the section somehow?**). Each space is later used to represent ionization
 343 electrons at different stages of the detection process: their creation in the gas,
 344 their final position when hitting the readout plane, and finally their representation
 345 in the discrete pad space.

346 Detector Space

347 The detector space \mathcal{D} represents the physical space of our detector. We de-
 348 scribe it using Cartesian coordinates (x, y, z) . The z -axis is the detector's axis of
 349 symmetry, with its negative direction aligned with the proton beam. The origin
 350 $(0, 0, 0)$ is located at the center of the irradiated target. The positive x -axis passes
 351 through the center of one the OFTPCs along the intersection of its two planes
 352 of symmetry. The y -axis is then chosen to maintain a right-handed coordinate
 353 system.

354 Since the detector has a hexagonal symmetry, we use only one of its sectors
 355 in this work – the first sector $\mathcal{D}_1 \subset \mathcal{D}$ which is defined by the condition:

$$(x, y, z) \in \mathcal{D}_1 \Leftrightarrow |y| \leq x \tan \frac{\pi}{6}. \quad (1.8)$$

356 Simulations in this sector can be applied to all sectors by rotating the coordinates
 357 accordingly. The volume of the OFTPC in this sector, which has the shape of
 358 a trapezoidal prism, has these boundaries:

$$x \in [x_{\min}, x_{\max}] = [6.51, 14.61] \text{ cm}, \quad (1.9)$$

$$z \in [z_{\min}, z_{\max}] = [-8, 8] \text{ cm}, \quad (1.10)$$

$$y_{\max}(x_{\min}) = -y_{\min}(x_{\min}) = 2.75 \text{ cm}, \quad (1.11)$$

$$y_{\max}(x_{\max}) = -y_{\min}(x_{\max}) = 7.45 \text{ cm}, \quad (1.12)$$

359 where $y_{\max}(x)$ is the maximal value of the y -coordinate for a given x . The read-
 360 out is located at $z = 8$ cm; for some purposes, we also define the distance to
 361 the readout $d_r = 8$ cm – z as an alternative to the z -coordinate. **Keeping this**
 362 **paragraph as it is because the OFTPC volume is distinct from the first sector**

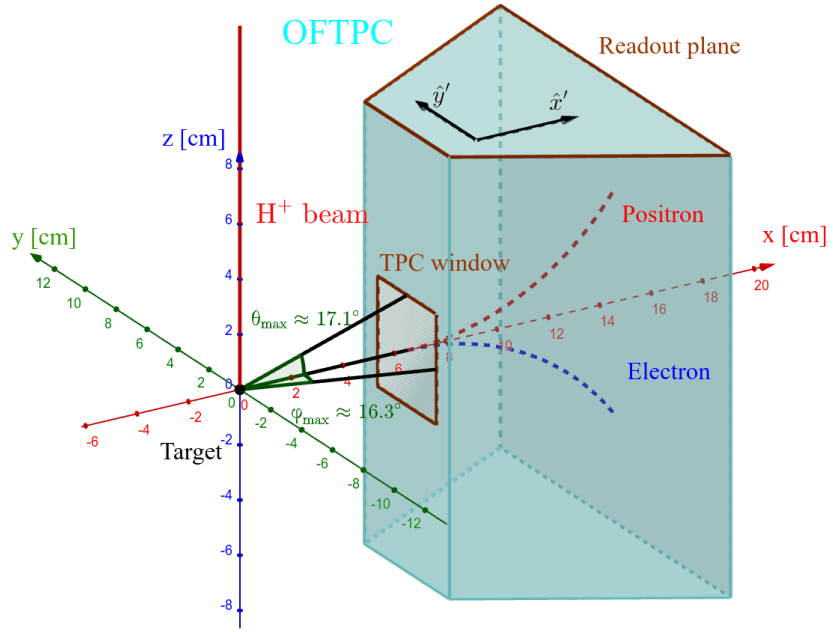


Figure 1.5: Schematics of the first sector OFTPC with detector space coordinates.

363 and some parts of this thesis use the space beyond this volume. The OFTPC
 364 window has width 3.8 cm and height 4.0 cm.

365 We also use spherical coordinates (r, θ, φ) with the elevation angle θ measured
 366 relative to the xy plane. Angles θ and φ are useful when describing the direction
 367 of e^+/e^- tracks. Their maximal values considered for the initial direction in
 368 simulations are $\theta_{\max} \approx 17.1^\circ$ and $\varphi_{\max} \approx 16.3^\circ$ as shown in Figure 1.5.

369 Readout Space

370 The readout space \mathcal{R} represents the drift time and final positions of ionization
 371 electrons as measured by an ideal continuous readout. We describe it using
 372 coordinates (x', y', t) , where x' and y' correspond to the detector coordinates at
 373 the readout plane ($z = 8$ cm).

374 Currently not entirely sure how to put this into a figure since only x' and
 375 y' correspond to the detector coordinates, **it will make more sense when**
 376 **visualizing the map**. The drift time t is approximately proportional to d_r .

377 Pad Space

378 The pad space \mathcal{P} represents the time bin and pad number of ionization electrons
 379 as measured by an ideal discrete readout:

$$\mathcal{P} = \{(n_{\text{pad}}, n_t) \in \mathbb{N}^2 \mid n_{\text{pad}} \leq 128\}. \quad (1.13)$$

380 **Rewrite to reflect this:** Technically both values can be zero as defined in
 381 the code (max channel 127). It is not really a subspace of \mathcal{R} but there is a
 382 mapping from \mathcal{R} to \mathcal{P} . It is a discretization of a part of \mathcal{R} , the mapping can be
 383 adjusted depending on the simulation. If we assume uniform electric field there
 384 will be gaps, we don't use gaps in the reconstruction since the electrons should
 385 be pulled towards the pads.

386 The readout of the OFTPC will consist (is the design final?) of 128 rectangular
 387 pads arranged in a staggered pattern. Parameters of the pad layout are shown
 388 in Figure 1.6. The bottom left corner of n -th pad has coordinates $(x_{1,n}, y_{1,n})$,
 389 the top right $(x_{2,n}, y_{2,n})$ and its center has coordinates $(x_{c,n}, y_{c,n})$. The gap
 390 between neighboring pads is $g = 0.08$ cm. Time will be read out in discrete bins
 391 of size $t_{\text{bin}} = 100$ ns (details?). Could also describe pad-related functions.

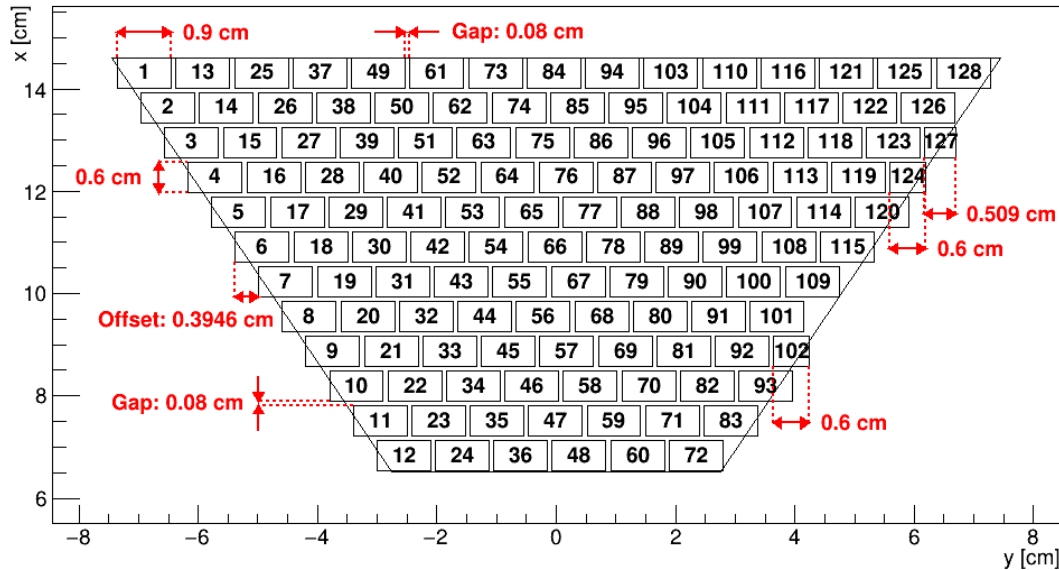


Figure 1.6: Pad layout of the OFTPC and its parameters. Pads 102, 124 and 127 are irregular, the rest has the same dimensions.

392 1.3.3 Magnetic Field Simulation

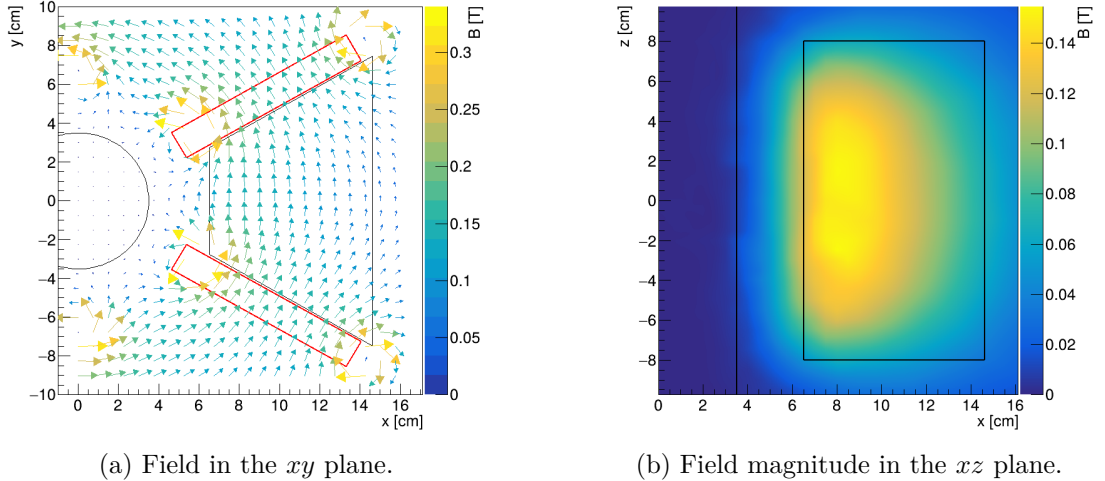
393 The magnetic field inside our detector is produced by six permanent magnets. It
 394 was simulated using Ansys Maxwell (citation) which gives us values on a regular
 395 grid. More details, vacuum tube, magnets (homogeneous?, density?). Visualization
 396 of the magnetic field is shown in Figure 1.7. Whenever we need to work with
 397 values outside this grid, we use trilinear interpolation described below.

398 Trilinear Interpolation

399 Trilinear interpolation is a 3D generalization of linear interpolation². It can be
 400 used to interpolate a function whose values are known on a regular grid with
 401 rectangular prism cells. We use this simple method for interpolating the magnetic
 402 field, and it is later used in Section 3.2.1 to interpolate the Ionization Electron
 403 Map, a key component of our track reconstruction algorithm. In both cases, we
 404 use a regular cubic grid (apparently it is also called a Cartesian grid).

405 Let us consider a cell of our regular grid (a cube) with an edge of length a
 406 containing the point $\mathbf{C} = (x, y, z)$ where we want to interpolate a function
 407 $f: \mathbb{R}^3 \rightarrow \mathbb{R}$. We know the values of this function at the vertices of the cell
 408 $\mathbf{C}_{ijk} = (x_0 + ia, y_0 + ja, z_0 + ka)$, where $\mathbf{C}_{000} = (x_0, y_0, z_0)$ is the origin of the cell

²Linear interpolation in point $x \in (x_1, x_2)$ of a function $f: \mathbb{R} \rightarrow \mathbb{R}$ known in points $x_1 < x_2$ is the convex combination $\hat{f}(x) = (1 - x_d)f(x_1) + x_d f(x_2)$, where $x_d = \frac{x - x_1}{x_2 - x_1} \in (0, 1)$.



(a) Field in the xy plane.

(b) Field magnitude in the xz plane.

Figure 1.7: Magnetic field simulation results. The OFTPC volume and the vacuum tube are marked with black lines, the magnets are marked with red lines. The coordinates of the magnets from the CAD drawing seem to be 9/10 of the ones from the magnetic simulation (confirm and fix).

409 (is that clear?), and $i, j, k \in \{0, 1\}$ are indices. We also define the points $\mathbf{C}_{ij} =$
410 $= (x, y_0 + ia, z_0 + ja)$ and $\mathbf{C}_i = (x, y, z_0 + ia)$. Then the interpolated value $\hat{f}(\mathbf{C})$
411 can be calculated as a composition of three linear interpolations (see Figure 1.8):

$$\hat{f}(\mathbf{C}_{ij}) = (1 - x_d) f(\mathbf{C}_{0ij}) + x_d f(\mathbf{C}_{1ij}), \quad (1.14)$$

$$\hat{f}(\mathbf{C}_i) = (1 - y_d) \hat{f}(\mathbf{C}_{0i}) + y_d \hat{f}(\mathbf{C}_{1i}), \quad (1.15)$$

$$\hat{f}(\mathbf{C}) = (1 - z_d) \hat{f}(\mathbf{C}_0) + z_d \hat{f}(\mathbf{C}_1), \quad (1.16)$$

412 where x_d , y_d , and z_d are given as follows:

$$x_d = \frac{x - x_0}{a}, \quad y_d = \frac{y - y_0}{a}, \quad z_d = \frac{z - z_0}{a}. \quad (1.17)$$

413 We can also write

$$\hat{f}(\mathbf{C}) = \sum_{i,j,k \in \{0,1\}} t_x^i t_y^j t_z^k f(\mathbf{C}_{ijk}), \quad (1.18)$$

$$t_\alpha \stackrel{\text{def}}{=} \begin{pmatrix} t_\alpha^0 \\ t_\alpha^1 \end{pmatrix} = \begin{pmatrix} 1 - \alpha_d \\ \alpha_d \end{pmatrix}, \quad (1.19)$$

414 where $\alpha \in \{x, y, z\}$ is an index. This gives a nice geometric interpretation to the
415 trilinear interpolation as shown in Figure 1.9. From this form and the figure, it
416 is apparent that the final interpolated value does not depend on the order of axes
417 along which we perform linear interpolations (see Figure 1.8). Furthermore, we
418 can write $\hat{f}(\mathbf{C})$ as a polynomial:

$$\hat{f}(\mathbf{C}) = \sum_{\alpha, \beta, \gamma \in \{0,1\}} \sum_{i=0}^{\alpha} \sum_{j=0}^{\beta} \sum_{k=0}^{\gamma} (-1)^{(\alpha-i)+(\beta-j)+(\gamma-k)} f(\mathbf{C}_{ijk}) x_d^\alpha y_d^\beta z_d^\gamma. \quad (1.20)$$

419 We take advantage of this form when generalizing trilinear interpolation to irreg-
420 ular grid in section 3.2.2.

421 Maybe a citation here, although I am not sure it is necessary since it could
422 be considered common knowledge. The last two equations are my own (but I'm
423 not sure that's worth mentioning unless there's a citation).

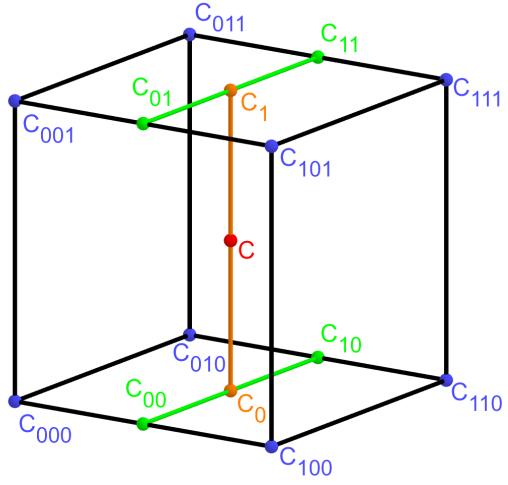


Figure 1.8: Visualization of trilinear interpolation as a composition of linear interpolations (inspired by [28]). We want to interpolate the value in the red point \mathbf{C} . First we interpolate between the four pairs of blue points sharing the last two indices along the x -axis (Eq. 1.14), then between the two pairs of the resulting green points along the y -axis (Eq. 1.15) and finally between the two resulting orange points along the z -axis to get the final red value (Eq. 1.16).

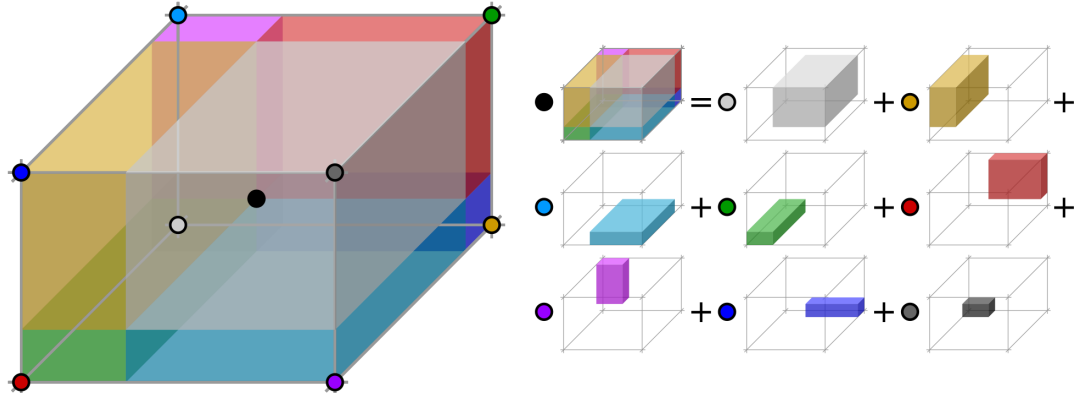


Figure 1.9: Geometric interpretation of trilinear interpolation as expressed in Equation 1.18. The colored dots represent the values in given points and the colored boxes represent the volume in the opposite corner by which the corresponding values are multiplied. The black dot represents the interpolated value which is multiplied by the entire volume [29].

2. Track Simulation

In order to develop and test the reconstruction algorithm, electron and positron tracks are simulated inside the first detector sector \mathcal{D}_1 (see Section 1.3.2) with different initial parameters (origin, initial direction and kinetic energy). Two approaches are currently used to simulate tracks, each of them for different purpose.

The **Microscopic Simulation** uses the Garfield++ toolkit [1]. Within this toolkit:

- a) Magboltz, since it is mentioned later
- b) the High Energy Electro-Dynamics (HEED) program [30] is used to simulate the primary particle,
- c) the class *AvalancheMicroscopic* to simulate the drift of secondary electrons created by ionization in the gas.

This is the most precise and time-consuming simulation used; our current goal is to be able to successfully reconstruct its results and determine our best-case energy resolution.

The **Runge-Kutta Simulation** uses the 4th order Runge-Kutta numerical integration (add citation for Runge-Kutta) to simulate the trajectory of the primary particle in the electromagnetic field inside the detector. It is relatively fast since it does not simulate the secondary particles. It is used as part of our reconstruction algorithm and for testing some parts of the reconstruction.

All of these simulations require the knowledge of the electromagnetic field (both **E** and **B**) inside the detector. A uniform electric field of $400 \text{ V}\cdot\text{cm}^{-1}$ is assumed. The magnetic field was simulated in Maxwell (see Section 1.3.3). add citation

Single track in positive x direction or initial parameter randomization. Importance of gas composition, used gas compositions.

2.1 Microscopic Simulation

The microscopic simulation, the most detailed simulation used in this work, is performed using the Garfield++ toolkit [1].

The electron transport properties are simulated using the program Magboltz (add citation, details?). Two different gas mixtures were compared – 90:10 and 70:30 Ar:CO₂. The second mixture will be used in our detector (this was probably known a priori, but the first tests that I started with used 90/10, so maybe just note that the results justify the fact so far). The temperature is set to 20 °C, the pressure is atmospheric.

The primary track is simulated using the program HEED, which is an implementation of the photo-absorption ionization model [30] (see the reference, moved it to the end of sentence). This program provides the parameters of ionizing collisions. HEED can also be used to simulate the transport of delta electrons; we do not account for these in the current simulation (but plan to include them in the future – maybe mention only in the conclusion/future section). The photons created in the atomic relaxation cascade (fluorescence reabsorption, ?) are also not simulated.

467 Finally, we use the microscopic tracking provided by the class *AvalancheMicroscopic*
 468 in Garfield++ to simulate the drift of the ionization electrons. Each
 469 electron is followed from collision to collision using the equation of motion and
 470 the collision rates calculated by Magboltz.

471 Add more detailed and better description of HEED, and microscopic tracking
 472 (each their own subsection?). Could also mention Monte Carlo (requires gas file
 473 generation - Magboltz) and Runge-Kutta simulation implemented in Garfield,
 474 why we don't use them (another subsection? rename the section to Garfield++
 475 simulation and mention all relevant parts?).

476 2.1.1 First testing track

477 The first electron track simulated for testing purposes was chosen to have a special
 478 set of parameters:

- 479 • the starting point of the track is the origin of the coordinate system,
- 480 • the initial direction is along the positive x -axis,
- 481 • the momentum is 8 MeV/c (the kinetic energy is 7.505 MeV).

482 Such a track moves in the XZ plane in the toroidal magnetic field of the detector,
 483 because the particle's velocity vector is always perpendicular to the field. At first,
 484 we simulated such a track in 90:10 Ar:CO₂ gas mixture, later we added a simu-
 485 lation in 70:30 Ar:CO₂, which we plan to use in our detector. The comparison of
 486 both simulations is in Figure 2.1.

487 2.1.2 Grid-like testing sample

488 In order to test all steps of the reconstruction, a sample of tracks with a grid-like
 489 distribution of parameters was generated on MetaCentrum. Five sets of 9702
 490 tracks were generated with every combination of these parameters:

- 491 • electron and positron tracks,
- 492 • 11 different kinetic energies $E_{\text{kin}} \in [3, 13]$ MeV,
- 493 • 21 different azimuth angles $\varphi \in [-16.3^\circ, 16.3^\circ]$ and
- 494 • 21 different elevation angles $\theta \in [-17.1^\circ, 17.1^\circ]$.

495 A visualization of a set of e^+/e^- tracks with the same kinetic energy is shown
 496 in Figure 2.2 (plotting actual HEED tracks using ROOT should be also possible
 497 (but hard to make look good?)). In the 70:30 Ar:CO₂ atmosphere, each track
 498 takes 5-30 CPU hours to simulate. Every tenth point on the drift line was stored,
 499 the whole sample has 3.1 terabytes (or 1.4 gigabytes without drift lines).

500 2.2 Runge-Kutta Simulation

501 The Runge-Kutta simulation in this work uses the Runge-Kutta 4th order (RK4)
 502 method to numerically integrate the equation of motion of a relativistic charged
 503 particle in an electromagnetic field. Given a system of first order differential
 504 equations

$$\frac{dy}{dt} = f(t, y(t)) \quad (2.1)$$

505 with an initial condition

$$y(t_0) = y_0, \quad (2.2)$$

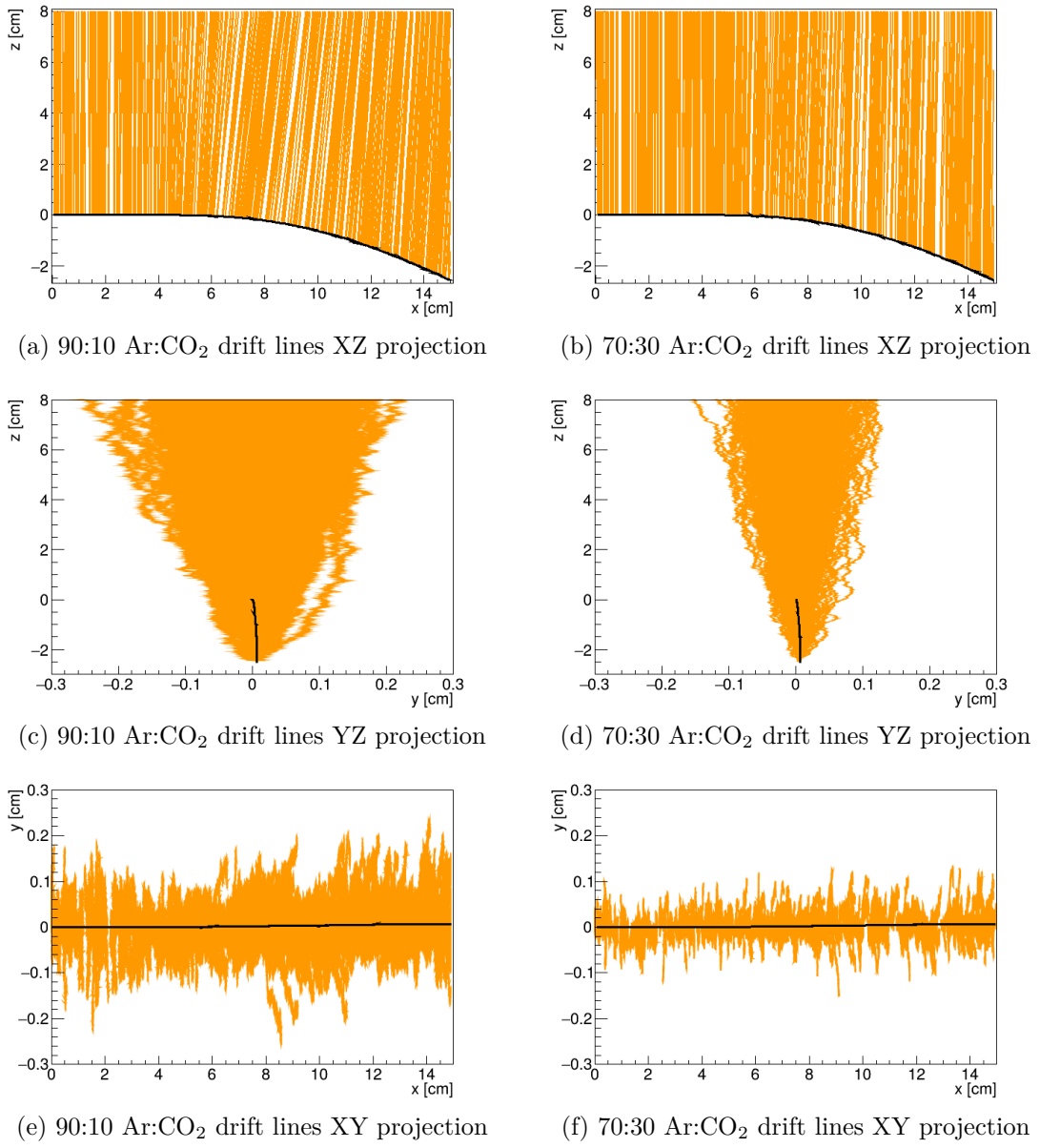


Figure 2.1: Comparison of drift lines for two different gas mixtures 90:10 and 70:30 Ar:CO₂. The electron track is marked in black, the drift lines of the ionization electrons are marked in orange. In this example, we assume a larger OFTPC volume with readout at $z = 8$ cm.

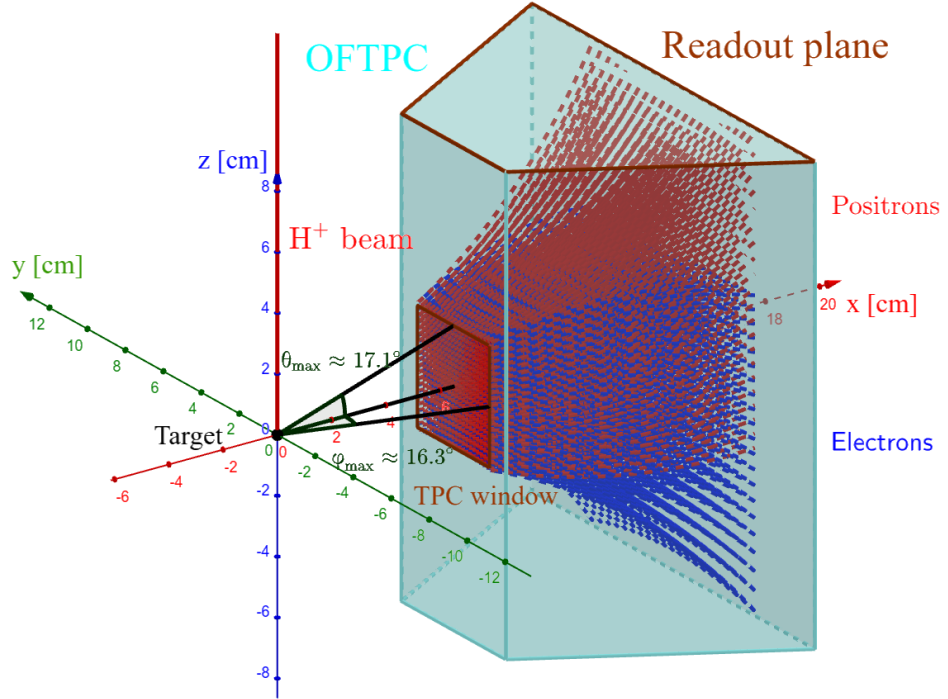


Figure 2.2: A visualization of a set of tracks from the grid-like testing sample with the same kinetic energy.

506 we iteratively compute the estimate $\mathbf{y}_n = \mathbf{y}(t_n) = \mathbf{y}(t_0 + nh)$ as follows (citation?
 507 common knowledge?):

$$\mathbf{k}_1 = \mathbf{f}(t_n, \mathbf{y}_n), \quad (2.3)$$

$$\mathbf{k}_2 = \mathbf{f}\left(t_n + \frac{h}{2}, \mathbf{y}_n + \frac{h\mathbf{k}_1}{2}\right), \quad (2.4)$$

$$\mathbf{k}_3 = \mathbf{f}\left(t_n + \frac{h}{2}, \mathbf{y}_n + \frac{h\mathbf{k}_2}{2}\right), \quad (2.5)$$

$$\mathbf{k}_4 = \mathbf{f}(t_n + h, \mathbf{y}_n + h\mathbf{k}_3), \quad (2.6)$$

508

$$\mathbf{y}_{n+1} = \mathbf{y}_n + \frac{1}{6}(\mathbf{k}_1 + 2\mathbf{k}_2 + 2\mathbf{k}_3 + \mathbf{k}_4). \quad (2.7)$$

509 Alternate forms (infinitely many) possible, accuracy vs computational cost. Runge-
 510 Kutta-Fehlberg with adaptive step size also possible, can potentially save some
 511 computation time especially in rapidly changing field (so maybe not in this case).

512 In our case, we want to integrate the equation of motion, given by the rela-
 513 tivistic Lorentz force:

$$F_L^\mu = m \frac{du^\mu}{d\tau} = q F^{\mu\nu} u_\nu, \quad (2.8)$$

514 where the Einstein summation convention is used, m is the mass of the particle,
 515 q is its charge, u^μ is its four-velocity, τ is the proper time (i.e., time in the particle's
 516 frame of reference) and $F^{\mu\nu}$ is the electromagnetic tensor at given coordinates x^μ
 517 (we consider it to be time-independent in our detector). Given the electric $\mathbf{E} =$
 518 $= (E_x, E_y, E_z)$ and the magnetic field $\mathbf{B} = (B_x, B_y, B_z)$ and using the metric

519 signature $(+, -, -, -)$, the equation expands to

$$\frac{d}{d\tau} \begin{pmatrix} \gamma c \\ \gamma v_x \\ \gamma v_y \\ \gamma v_z \end{pmatrix} = \frac{q}{m} \begin{pmatrix} 0 & -\frac{E_x}{c} & -\frac{E_y}{c} & -\frac{E_z}{c} \\ \frac{E_x}{c} & 0 & -B_z & B_y \\ \frac{E_y}{c} & B_z & 0 & -B_x \\ \frac{E_z}{c} & -B_y & B_x & 0 \end{pmatrix} \begin{pmatrix} \gamma c \\ \gamma v_x \\ \gamma v_y \\ \gamma v_z \end{pmatrix}, \quad (2.9)$$

520 where c is the speed of light in vacuum, $\mathbf{v} = (v_x, v_y, v_z)$ is the particle's velocity
 521 and $\gamma = (1 - \frac{v^2}{c^2})^{-\frac{1}{2}}$ is the Lorentz factor (wrong magnetic field sign in the
 522 implementation???). Together with the equation

$$\frac{d}{d\tau} \begin{pmatrix} ct \\ x \\ y \\ z \end{pmatrix} = \begin{pmatrix} \gamma c \\ \gamma v_x \\ \gamma v_y \\ \gamma v_z \end{pmatrix} = u^\mu, \quad (2.10)$$

523 we get a system of eight first order differential equations for x^μ and u^μ , which
 524 we can integrate using the Runge-Kutta method described above. As a result of
 525 this integration, we get the position $\mathbf{x}(\tau_n)$, the velocity $\mathbf{v}(\tau_n)$ and the detector
 526 time $t(\tau_n)$ for every proper time $\tau_n = n\tau_{\text{step}}$. Integrating using the proper time
 527 means that the step size in t gets larger by the gamma factor $\frac{dt}{d\tau} = \gamma$ (maybe
 528 change it and integrate the detector time or adjust the step size accordingly). The
 529 only difference is in the step size (because t gets also calculated as it is among the
 530 8 variables). It might be even better to adjust the step size using approx-
 531 imate distance traveled. As initial conditions, we use the origin of the track
 532 (x_0, y_0, z_0), the initial velocity direction vector $\mathbf{n} = (\cos \varphi \cos \theta, \sin \varphi \cos \theta, \sin \theta)$
 533 and the kinetic energy E_{kin} (initial parameters of the simulation (fit is in chap-
 534 ter 4)), we then compute γ and $\|\mathbf{v}\|$:

$$\gamma = 1 + \frac{E_{\text{kin}}}{E_0}, \quad (2.11)$$

$$\|\mathbf{v}\| = c\sqrt{1 - \gamma^{-2}}. \quad (2.12)$$

535 2.2.1 Testing sample

536 Example of RK simulation – first testing track, randomized sample of 100000
 537 tracks (could also move them to circle 3D fit).

538 In order to test the simulation and reconstruction, a sample of 100 000 tracks
 539 with randomized parameters was generated:

- 540 • the Runge-Kutta step was set to 0.1 ns (proper time, which wouldn't be a
 541 problem but this way the "spatial" step depends on energy),
- 542 • the kinetic energy of the particle $E_{\text{kin}} \in [4, 12]$ MeV,
- 543 • the starting point of the track is a random point in the OFTPC window,
- 544 • the initial direction is given by the line connecting a random point on
 545 the target¹ (a disc with 1 mm radius in the YZ plane).

¹To generate a random point on the target, we generate a random angle α and a random square of the distance from origin r^2 to get a uniform distribution.

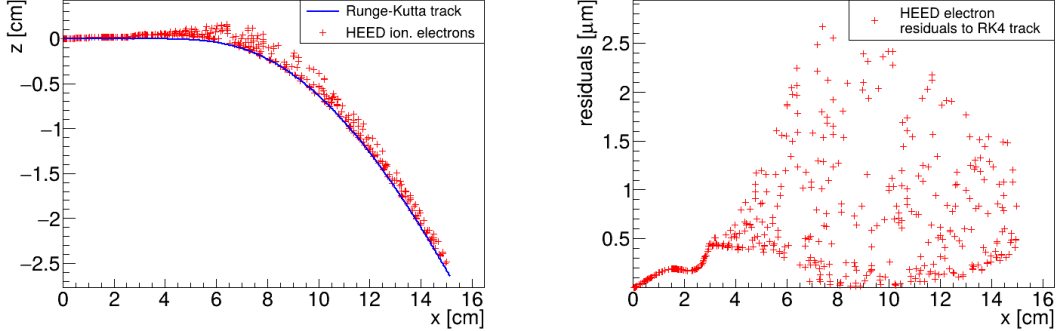


Figure 2.3: A comparison of the HEED track from the microscopic simulation in Section 2.1.1 with a Runge-Kutta track with the same initial parameters and $\tau_{\text{step}} = 0.1 \text{ ps}$ (reducing the step further doesn't make a visible difference). In the view of the tracks on the left, the distance of the HEED ionization electrons from the RK4 track is exaggerated 1000 \times . On the right, the dependence of the HEED electrons residuals (i.e., their shortest distance to the RK4 track) on their z -coordinate is shown. **The images look the same even for 100,000x smaller step, so the residuals are a result of something that HEED does.**

When exaggerating, the HEED ionization electrons are moved away along the shortest line connecting them to the RK4 track. The computation of this distance is described in Section 4.3.

546 Since the Runge-Kutta simulation is quite fast², it can be run locally on any
547 computer. **Add a figure with simulated tracks (sample).** An example Runge-
548 Kutta track is compared with the corresponding microscopic track in Figure 2.3.

²One track with $\tau_{\text{step}} = 0.1 \text{ ps}$ takes less than one millisecond to simulate.

3. Track Reconstruction

As the first step of the reconstruction algorithm, we reconstruct the track of a primary particle – either an electron or a positron. Then, using this information, we determine the energy of the particle (Section 4).

The **Reconstruction Assuming Steady Drift** uses the standard TPC approach. With parallel fields, the drift inside a uniform electric field remains undistorted (as shown in Equation 1.1). Therefore, we only need to reconstruct the z -coordinate from the drift time using the known drift velocity. We also assume that the readout coordinates (x' , y' , t) are known exactly, neglecting the pads and time binning.

Reconstruction using an **Ionization Electron Map** (from now on referred to as *the map*) uses a simulation of the drift of secondary (ionization) electrons within the detector volume. This simulation can then be used to interpolate the initial position of the secondary electrons. In the first iteration of this method the readout is assumed to be continuous.

We present two algorithms using the map for reconstruction. The first one uses a gradient descent algorithm along with trilinear interpolation (see Section 1.3.3) of the map. The second method uses interpolation on the irregular inverse grid with a polynomial.

The **Discrete Reconstruction** uses the map; instead of reconstructing the exact position of each electron, we reconstruct the center of each hit pad together with the time corresponding to the midpoint of the time bin. The electron count in each TPC bin (consisting of the pad and the time bin) serves as an idealized collected charge, which is then used as a weight in the energy reconstruction fit.

3.1 Reconstruction Assuming Steady Drift

As the first step, we tried to reconstruct a simulated electron track with a special set of initial parameters, described in detail in Section 2.1.1. The starting point is given by the origin of our coordinate system and its initial direction is given by the positive x -axis. This means the magnetic field of our detector is perpendicular to the momentum of the particle at all times, and we can reduce the problem to two-dimensional space.

For the reconstruction, we decided to use the common method used in a standard TPC ([similar to?](#)). This will allow us to explore the significance of the atypical behavior in our OFTPC. Additionally, we assume the readout is continuous to further simplify the problem. In this approximation, we reconstruct the initial position of each ionization electron.

The reconstruction is then defined by the following relations between the coordinates of the detector space and the readout space (see Section 1.3.2): ([some figure, maybe already relating to some track so that it's not too dull](#))

$$x = x', \quad (3.1)$$

$$y = y', \quad (3.2)$$

$$z = v_d t, \quad (3.3)$$

588 where v_d is the drift velocity of electrons in the given gas mixture. At a phe-
 589 nomenological level, this velocity can be considered as a function of the electric
 590 field \mathbf{E} and the magnetic field \mathbf{B} as shown in Equation 1.1. The Garfield++
 591 toolkit uses this fact to accelerate their drift simulation with non-microscopic
 592 approaches (could mention in the simulation chapter). Since we assume a uni-
 593 form electric field in the detector and in this approximation we want to neglect
 594 the effect of our unusual magnetic field, we consider the drift velocity constant.
 595 **Rewrite this while making figures:** We then approximate this velocity by
 596 fitting the dependence $z(t)$ taken from the simulated ionization electrons. This
 597 is in one of the provisional figures. Also, this description is not completely ac-
 598 curate; in reality, we fit $t1:8-y0$ with $a1*x+a0$ and then invert this and use $8-y0$
 599 $= b1*t1+b0$ (old coordinates); $b1=1/a1$ functions as the drift velocity. Maybe
 600 also define this $8-z$ variable as an alternative to z in Section 1.3.2 and then use it
 601 when correcting this.

602 Later, in a commit after this, I plotted some residues (provisional figure),
 603 which could be useful, but for some reason they are residuals from a spline fit of
 604 the track?! Probably redo this without the spline fit; just explore the difference
 605 in individual points.

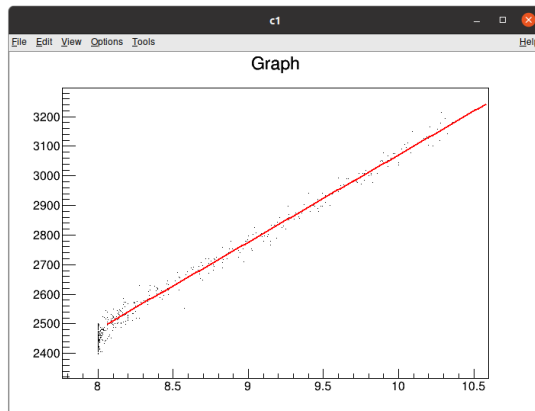


Figure 3.1: Dependence of the drift time on the z coordinate in 90 % argon and 10 % CO₂ atmosphere, fitted with a linear function. The fitted function gives us the average drift velocity in the gas and can be used for rough reconstruction in our TPC. Swap for better image with axis labels, etc. Maybe write the fitted equation.

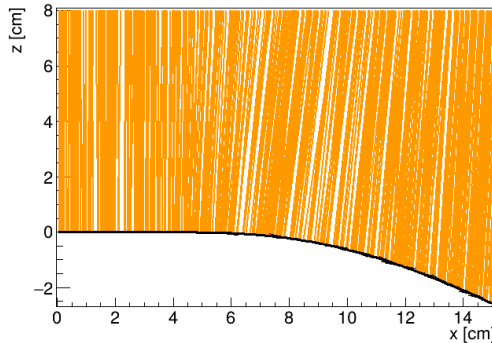


Figure 3.2: The first attempt of a track reconstruction using only the drift velocity. This approach works well in a standard TPC (ideally cite some source). 90 % argon and 10 % CO₂ atmosphere. Swap for better image, correct coordinates.

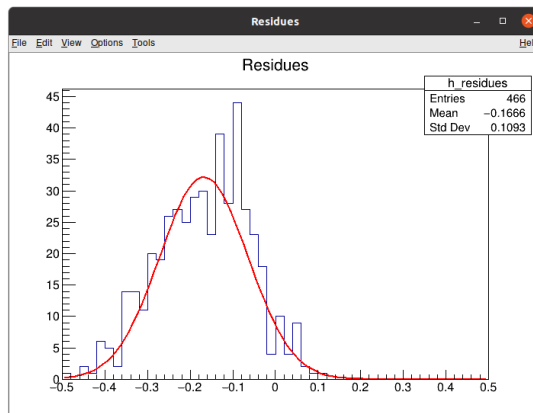


Figure 3.3: First attempt at a track reconstruction using only the drift velocity, residues. Swap for better image, correct coordinates. What's causing the shift? Explain details.

606 3.2 Ionization Electron Map

607 Inside an OFTPC (**more than one, also considering it a general concept rather**
 608 **than the specific OFTPC used at this experiment**), the drift of the secondary
 609 (ionization) electrons is significantly affected by its magnetic field (**pictures of**
 610 **the distortion later, the effect is bigger for the 90/10 composition.**). We need to
 611 take this into account for accurate reconstruction (should be easy to run the re-
 612 **construction without the map and show how much it improves the results**). In
 613 the first approximation, we assume a continuous readout (i.e., we neglect the an-
 614 ode segmentation into pads). We can then reconstruct the original position of
 615 each ionization electron using its readout coordinates. For this purpose, we use
 616 the ionization electron map.

617 The ionization electron map represents a mapping from the detector space
 618 to the readout space (see Section 1.3.2). It tells us what readout coordinates
 619 (x', y', t) we can expect on average for an ionization electron created at the de-
 620 tector coordinates (x, y, z). More precisely, it is a mapping to the distributions

on the readout space; we can simplify this as only the means $\bar{\mathcal{M}}$ (inconsistent notation in the text, write the bar everywhere or nowhere) and the covariance matrices \mathcal{M}_{cov} , assuming Gaussian distribution (test this – some chisq or other statistical test).

$$\bar{\mathcal{M}} : \mathcal{D} \longrightarrow \mathcal{R}, (x, y, z) \longmapsto (\bar{x}', \bar{y}', \bar{t}). \quad (3.4)$$

To get an approximation of this mapping, we simulate the drift of ionization electrons generated on a regular grid inside the volume of our OFTPC¹. In order to get accurate results, we use the microscopic simulation of these electrons described in Section 2.1 (Monte Carlo from *AvalancheMC* was also considered but it doesn't (didn't?) include magnetic field, we can probably improve this anyway using the fast track simulation with map proposed in the future section). It is also useful to simulate multiple (100 in our case, this should really only be in a table since there are two map simulations) electrons originating from the same position so that we can account for the random fluctuations due to collisions.

When evaluating the map inside the grid, we use trilinear interpolation (see Section 1.3.3). From now on, we will use the same symbol \mathcal{M} for this interpolated simulation.

Finally, we need to invert the map to get the original detector coordinates (x, y, z) from the given readout coordinates (x', y', t) . In our case, it is reasonable to assume that the mapping $\bar{\mathcal{M}}$ (of means (notation inconsistency), we lose the information about the distribution (a wild idea how to recover this is in the Future section but it will only make sense if the GEM is already accounted for and is very preliminary as there are many factors to consider)) is one-to-one (as seen in the simulations). We implemented two methods for this purpose: the gradient descent search (Section 3.2.1) and interpolation on the inverse grid (Section 3.2.2).

The simulation (?) of the map is a computationally heavy task. For this reason, we use the MetaCentrum grid [3] to parallelize needed calculations. At first, this was done by evenly distributing the simulated electrons across the individual jobs in a simulation with only one electron per vertex in the regular grid with a spacing of one centimeter. Later, a more efficient approach was implemented, accounting for the varying lengths of the drift of individual electrons. If we index the electrons in the order of increasing coordinates y, x, z (picture will make things clearer), we can express the number n_l of full XY layers (i.e., electrons with the same z coordinate) of electrons with index less than or equal to i

$$n_l(i) = \left\lfloor \frac{i}{n_{xy}} \right\rfloor, \quad (3.5)$$

where n_{xy} is the number of electrons in each XY layer calculated simply by counting the electrons that satisfy boundary conditions for x and y . These conditions should be mentioned above; sector condition + maximal x value. The number of electrons remaining in the top layer is then

$$n_r(i) = i \bmod n_{xy}. \quad (3.6)$$

Finally, we can calculate the sum of the drift gaps of electrons up to index i

$$d_{\text{sum}} = (z_{\max} - z_{\min})n_{xy}n_l - \frac{n_l(n_l - 1)}{2}n_{xy}l + n_r(z_{\max} - z_{\min} - n_l l). \quad (3.7)$$

¹The detector walls are not considered and we simulate the drift even outside of the OFTPC which allows us to interpolate even close to the walls

659 We then use a binary search algorithm to find the maximum index i such that
660 the value of this sum is less than the fraction $\frac{\text{job id}}{\max \text{job id}}$ of the total sum. This way
661 we obtain the minimal and the maximal index of electrons simulated in the given
662 job. The spacing l should be probably defined above + picture of the simulating
663 grid (1 layer). zmin zmax also

664 After the simulation of the map, we calculate the mean readout coordinates
665 assuming Gaussian distribution (i.e., we use averages). We also calculate standard
666 deviations in a later commit, should be upgraded to the covariance matrix. We
667 never actually plotted the distributions we get when simulating the same electron
668 multiple times, so we do not know if our assumptions are accurate (could also
669 run some statistical test to see how well the Gaussian distribution fits).

670 The obtained map is then stored in a custom class template *Field*, could
671 expand on that. Maybe earlier, since the same template is used for the magnetic
672 field.

673 Could insert a table here describing all 4 simulations of the map (gas composi-
674 tion, spacing, etc.). Simulation inside of one sector (at first double angle). Extra
675 space on the sensor. Edge cases not taken into account (TPC wall). Using qsub
676 (not sure if important). Add plots of distortion of the coordinates. Could also do
677 these plots in a different way (e.g., drawing all the endpoints of each ionization
678 electron or some error ellipse plot).

679

680 Images to add (comparison of both simulations):

- 681 • Already have a simple 2D map visualization from the RD51 presentation,
682 can use it or make something better
- 683 • 3D visualization of the map, simulation example
- 684 • z vs. t plot
- 685 • XY plane distortion for different z values; with arrows and error bars, for
686 all z -layers with different colors
- 687 • XZ plane ($y = 0$) distortion in x (maybe not necessary?)
- 688 • XT plot ($y = 0$) showing (small) distortion in drift times

689

690 More images:

- 691 • Residuals of the continuous readout reconstruction.

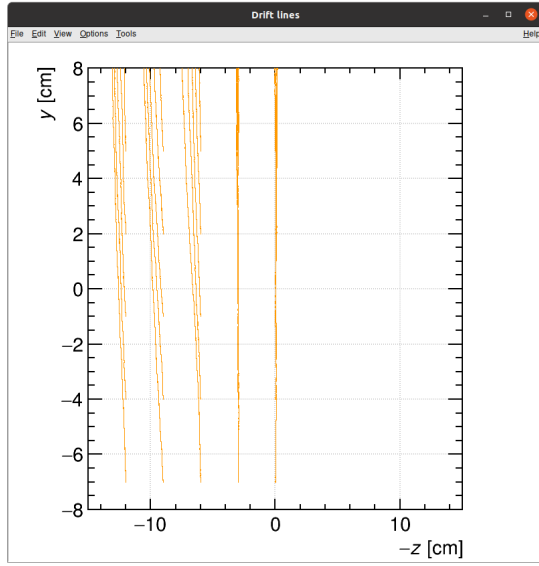


Figure 3.4: Example of map generation. Swap for better image, correct coordinates.

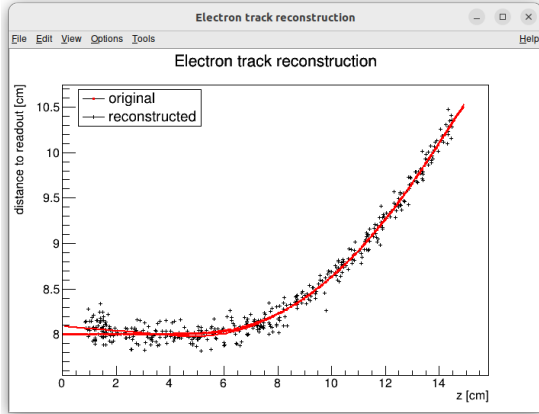


Figure 3.5: Example reconstruction with the map. Swap for better image, correct coordinates.

692 3.2.1 Gradient Descent Algorithm

693 The first implemented method of reconstruction uses a gradient descent algorithm
 694 to calculate an inversion of the map $\bar{\mathcal{M}}$ in a given point. Gradient descent is
 695 an iterative minimization algorithm for multivariate functions. Let $R \in \mathcal{R}$ be
 696 a point in the readout space; we want to find a point $D = (x, y, z) \in \mathcal{D}$ in
 697 the detector space such that

$$\bar{\mathcal{M}}(D) = R = (x'_R, y'_R, t_R). \quad (3.8)$$

698 We define a function f_R in the readout space as a distance in this space:

$$f_R(x', y', t) = \sqrt{(x' - x'_R)^2 + (y' - y'_R)^2 + v_d^2(t - t_R)^2}, \quad (3.9)$$

699 where v_d is an approximation of the drift velocity in the TPC, obtained from
 700 the reconstruction in Section 3.1 (there will be an image with the linear fit here).

701 We make an initial guess (actually in the original code we just take $z = 0$):

$$D_0 = (x'_R, y'_R, v_d t). \quad (3.10)$$

702 Assuming we have the n -th estimate D_n , we calculate the i -th component of
703 the gradient of $f_R \circ \bar{\mathcal{M}}$ numerically using central differences: (signs look correct)

$$[\nabla(f_R \circ \bar{\mathcal{M}})]^i(D_n) \approx \frac{f_R(\bar{\mathcal{M}}(D_n + s \cdot e^i)) - f_R(\bar{\mathcal{M}}(D_n - s \cdot e^i))}{2s}, \quad (3.11)$$

704 where $e^i \in \mathcal{D}$ is the i -th coordinate vector and s is the step size. The step size
705 should be sufficiently small; initially, we set it as a fraction $s = \frac{l}{10}$ of the map's
706 grid spacing l . During the minimization, we check that $f_R(\bar{\mathcal{M}}(D_n)) < 10s$ at all
707 times (s can (?) change – check). When using trilinear interpolation, it would be
708 more efficient to calculate the gradient explicitly (\pm same result). This could be
709 implemented inside the *Field* template class. The next iteration can be calculated
710 as follows:

$$D_{n+1} = D_n - \gamma \nabla(f_R \circ \bar{\mathcal{M}})(D_n), \quad (3.12)$$

711 where $\gamma \in \mathbb{R}^+$ is the damping coefficient. It should be set to a small enough
712 value to ensure convergence, but large enough for sufficient converging speed.
713 The minimization stops either when the error $f_R(\bar{\mathcal{M}}(D_n))$ drops below a specified
714 value or when the number of iterations exceeds a certain limit (in this case,
715 a message is printed into the console). The parameters of this method can be
716 further optimized (e.g., a better choice of γ , gradient computation); instead, we
717 later decided to use the interpolation on the inverse grid described in the next
718 section.

719 Measure reconstruction duration and compare it with the inverse grid inter-
720 polation? Also compare the result? Typical evolution of D_n during search. Not
721 sure if this has to be cited.

722 3.2.2 Interpolation on the Inverse Grid

723 Interpolation should be generally faster than the gradient descent since we don't
724 need to iterate. We also don't need to optimize it to improve performance, if
725 it's too slow we can even calculate the coefficients for the entire map before
726 reconstruction (again, do some profiling).

727 The best current algorithm uses the interpolation on the inverse grid. Rather
728 than inverting the trilinearly interpolated map using a numerical minimization
729 method as in the previous section, we take advantage of the fact that the map
730 $\bar{\mathcal{M}}$ is one-to-one (isomorphism is supposed to preserve structure, not sure how
731 to interpret that here, not the best description, we already (kind of) assume it
732 is a bijection by saying we will invert it). Since we have simulated values of this
733 map on a regular grid in the detector space \mathcal{D} , we also know the inverse map $\bar{\mathcal{M}}^{-1}$
734 on the irregular inverse grid in the readout space \mathcal{R} . To get an approximation
735 of the inverse map in the entire readout space, we can use interpolation (general
736 concept, the specific choice is described below).

737 Since the inverse grid is irregular, trilinear interpolation cannot be applied.
738 Given that the simulated map is dense enough to provide a good approximation

739 considering the size of our pads, we can adopt a similar approach.² As shown in
 740 Equation 1.20 in Section 1.3.3, trilinear interpolation (**shouldn't need an article**
 741 **when talking about a general concept**) can be expressed as a polynomial:

$$\hat{f}(x, y, z) = axyz + bxy + cxz + dyz + ex + fy + gz + h, \quad (3.13)$$

742 where a, b, c, d, e, f, g, h are coefficients uniquely determined by the values of
 743 the function at the vertices of the interpolation cell (**can be calculated in the**
 744 **way shown in the mentioned equation, not sure what more to add**). We can gen-
 745 eralize this for a function defined on an irregular grid. Given the function values
 746 at any eight points, we can write a system of eight linear equations

$$\begin{pmatrix} x_1y_1z_1 & x_1y_1 & x_1z_1 & y_1z_1 & x_1 & y_1 & z_1 & 1 \\ \vdots & \vdots \\ x_8y_8z_8 & x_8y_8 & x_8z_8 & y_8z_8 & x_8 & y_8 & z_8 & 1 \end{pmatrix} \begin{pmatrix} a \\ \vdots \\ h \end{pmatrix} = \begin{pmatrix} f(x_1, y_1, z_1) \\ \vdots \\ f(x_8, y_8, z_8) \end{pmatrix}, \quad (3.14)$$

747 which has a unique solution for the coefficients for most values of (x_n, y_n, z_n) and
 748 $f(x_n, y_n, z_n)$, where $n \in \{1, \dots, 8\}$.

749 This approach introduces a small complication: finding the correct pseudocell
 750 (i.e., the image of eight vertices forming a cubic cell in the regular grid) in
 751 the inverse grid. The eight irregularly spaced vertices of this pseudocell do not
 752 define a unique volume, so there are multiple possible ways to partition \mathcal{R} into
 753 pseudocells, with no obvious choice among them.

754 We are currently ignoring this problem and performing binary search along
 755 x, y, z (in this order). It shouldn't matter too much because the 70/30 map
 756 doesn't cause such a big distortion and was even accidentally extrapolated for all
 757 z different from the central plane.

²A more complicated and computationally heavy alternative would be natural neighbor interpolation or Kriging.

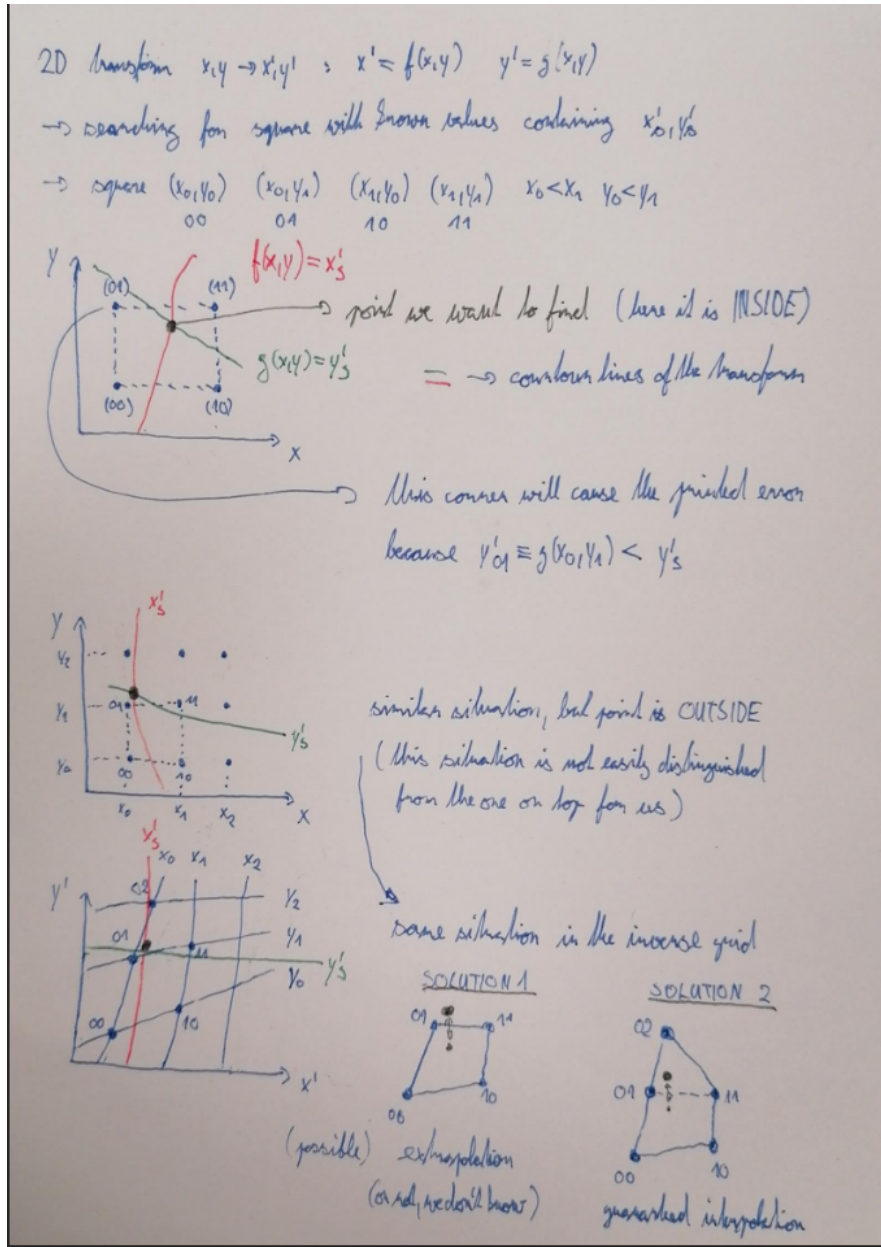


Figure 3.6: Selection of the points for interpolation. Create better images; use the explanation interpolation vs. extrapolation strange property. Solution 2 probably does not make much sense.

758 3.3 Discrete Reconstruction

759 Reconstruction with pads and time bins. Maybe testing different pads.

760 It is also possible to make this a subsection of the map, making the previous
761 subsections parts of a new subsection 'Map Inversion'.

762 In order to get a more realistic representation of a track measured in the OFTPC,
763 we need to take the discretization of the position and time data into account.
764 The readout of the OFTPC will consist of 128 pads, their layout is shown in
765 Figure 1.6. Time is read out in discrete bins of size $t_{\text{bin}} = 100$ ns.

766 As the first approximation, we can neglect the multiplication in the triple-GEM.

767 and assume an ideal charge readout. The time measurement starts at the begin-
 768 ning of the electron/positron simulation (depending on the specific simulation it
 769 can correspond to the production in the target or when entering the OFTPC,
 770 here the specific time doesn't matter too much since the primary particle trav-
 771 els basically at light speed (30 ps/cm) which is circa immediate given the time
 772 binning). Randomize this time a bit and see what it does to the reconstruction.
 773 The readout coordinates $(x', y', t) \in \mathcal{R}$ of each ionization electron can be mapped
 774 to the pad coordinates $(n_{\text{pad}}, n_t) \in \mathcal{P}$:

$$n_{\text{pad}} = n: (x', y') \in \left[x_{1,n} - \frac{g}{2}, x_{2,n} + \frac{g}{2} \right] \times \left[y_{1,n} - \frac{g}{2}, y_{2,n} + \frac{g}{2} \right], \quad (3.15)$$

$$n_t = \left\lceil \frac{t}{t_{\text{bin}}} \right\rceil, \quad (3.16)$$

775 where $x, y_{1,n}$ and $x, y_{2,n}$ are the opposing pad corner coordinates, and g is the
 776 gap between the pads (described in detail in Section 1.3.2). This way, the closest
 777 pad is assigned to each readout position within the OFTPC volume³. Makes
 778 sense since the pads attract the electrons, the inhomogeneity of electric field is
 779 neglected. The number of electrons collected by each pad (i.e., collected charge)
 780 in each time bin is then counted and serves as a weight for the energy recon-
 781 struction. The reconstructed track consists of points for each $(n, n_t) \in \mathcal{P}$, we get
 782 these by reconstructing the position of a hypothetical electron with the readout
 783 coordinates of the pad/time bin center:⁴

$$\mathcal{D} \ni (x, y, z) = \overline{\mathcal{M}} \left(x_{c,n}, y_{c,n}, \left(n_t - \frac{1}{2} \right) t_{\text{bin}} \right). \quad (3.17)$$

³Some positions near the wall are not handled and some pads extend beyond the OFTPC volume. This is where an electric field simulation would come in handy.

⁴Mapping the center of the pad (along with the midpoint of the time bin) isn't necessarily the best approach since it might not correspond to the average parameters of an electron with these readout parameters.

4. Energy Reconstruction

The second stage is the reconstruction of the particle's energy using a fit of its reconstructed track (see Section 3). We have tested three ways of reconstructing the energy. Fitting is done using the MINUIT algorithm implemented in ROOT [2]. Cite some CERN article directly on MINUIT, can add a section. Or is it done using MIGRAD? The circle and RK4 probably was.

The **Cubic Spline Fit** was a tested and later rejected method of energy reconstruction. It uses smoothly connected piecewise cubic polynomials between uniformly spaced nodes. The reconstructed energy is calculated using the fit parameters by computing the radius of curvature in different points of the fitted curve using the known magnitude of the magnetic field perpendicular to the trajectory. We rejected this method because the tuning of the fit turned out to be unpractical compared to the other used methods. Reconstructs energy at every position (even though the actual energy doesn't change much) and it might be slower but no profiling has been done yet. Of course, it wasn't tested on the newer track reconstruction methods at all.

The **Circle and Lines Fit** was chosen as an alternative since this corresponds to the shape of a trajectory of a charged particle crossing a finite volume with a homogeneous magnetic field. The energy of the particle can be estimated using the fitted radius and the magnitude of the perpendicular magnetic field in the middle of the TPC.

The **Runge-Kutta Fit** uses the 4th order Runge-Kutta numerical integration described in Section 2.2. Initial parameters of the track (including the particle's energy) are optimized so that the integrated trajectory fits to the reconstructed one. This fit can also be performed as a single parameter (i.e., energy) fit if we get the initial position and orientation of the particle on the entrance to the TPC from previous detectors (TPX3 and MWPC, see Section 0.2).

4.1 Cubic Spline Fit

The first method for the estimation of the kinetic energy of the particle uses a cubic spline fit. We use an electron track simulated using the microscopic

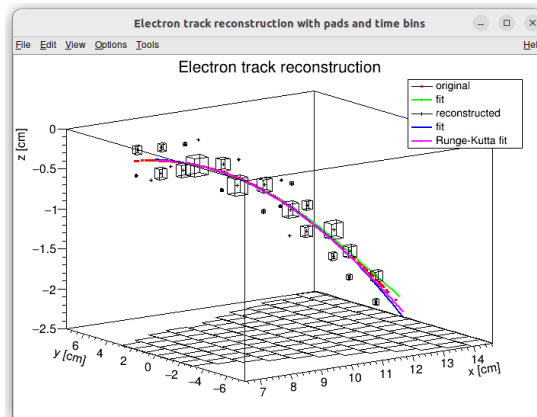


Figure 4.1: Example of a fitted reconstructed track. Swap for better image.

simulation, described in detail in Section 2.1.1. The track was reconstructed using the map described in Section 3.2.

In order to calculate the spline, we use the class *TSplines3* from ROOT. This allows us to evaluate the spline using the coordinates (x_n, z_n) of each node and the derivatives d_1, d_2 in the first and the last node. We can fit these parameters of a fixed amount of nodes to the simulated trajectory. We use the IMPROVE algorithm provided by the *TMinuit* class in ROOT (there are some guidelines for fonts in MFF UK template (Czech version) that I will eventually apply (see notes in the conclusion)). This algorithm attempts to find a better local minimum after converging (could reformulate a bit, taken word for word from some manual).

After the fit converges, we calculate an energy estimate using the radius of curvature, which we can extract from the fitted spline equation at every point of the trajectory. The part of the spline corresponding to a given node is defined as

$$z(x) = z_n + b\Delta x + c(\Delta x)^2 + d(\Delta x)^3, \quad (4.1)$$

where $\Delta x = x - x_n$ and b, c, d are coefficients. Using this equation, we derive the radius of curvature¹ as:

$$r(x) = \frac{(1 + z'^2(x))^{\frac{3}{2}}}{z''(x)} = \frac{(1 + (b + 2c\Delta x + 3d(\Delta x)^2)^2)^{\frac{3}{2}}}{2c + 6d\Delta x}. \quad (4.2)$$

Based on the geometry of our detector, we assume that the magnetic field satisfies $\mathbf{B}(x, 0, z) = (0, B(x, z), 0)$ for a track in the XZ plane. Since the electron is relativistic, the effect of the electric field on its trajectory is negligible. The Lorentz force F_L is then always perpendicular to the momentum of the electron and acts as a centripetal force F_c (not quite sure how to handle this then?):

$$\begin{aligned} \mathbf{F}_L &= \mathbf{F}_c, \\ \|e\mathbf{v} \times \mathbf{B}\| &= \frac{\gamma m_e v^2}{r}, \\ ec\beta B &= \frac{E_{0e}\beta^2}{r\sqrt{1 - \beta^2}}, \end{aligned} \quad (4.3)$$

$$\sqrt{1 - \beta^2} = \frac{E_{0e}\beta}{ecBr}, \quad (4.4)$$

$$\beta^2(x) = \left[1 + \left(\frac{E_{0e}}{ecB(x, z(x))r(x)} \right)^2 \right]^{-1}, \quad (4.4)$$

where e is the elementary charge, c is the speed of light in vacuum, m_e is the rest mass of electron, $E_{0e} = m_e c^2$ is its rest energy, γ is the Lorentz factor, \mathbf{v} is the velocity of the electron, and $\beta = \frac{v}{c}$. The kinetic energy for a given point on the trajectory is then given as

$$E_{\text{kin}}(x) = \left(\frac{1}{\sqrt{1 - \beta^2(x)}} - 1 \right) E_{0e}. \quad (4.5)$$

¹For the general formula see https://en.wikipedia.org/wiki/Curvature#Graph_of_a_function.

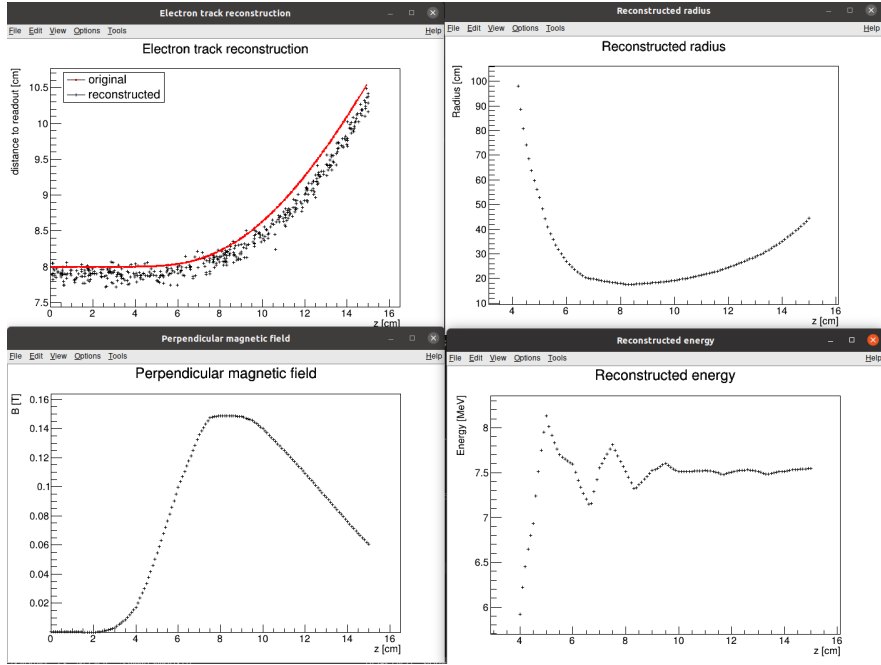


Figure 4.2: First attempt at a track reconstruction using only the drift velocity. Spline energy reconstruction attempt. Swap for better image(s) – subfigure environment, correct coordinates.

838 We can then average these estimates at multiple points (possibly using some
 839 weights to account for the change in accuracy, this wasn't optimized and we just
 840 ended with the graph) to get a single value. This method was later rejected in
 841 favor of the circle and lines fit the name was already established at the beginning
 842 of the chapter described in the next section. Add some figures.

843 4.2 Circle and Lines Fit

844 Another way to estimate the particle's kinetic energy is to fit its (??) trajectory
 845 with a circular arc with lines attached smoothly. This shape of trajectory cor-
 846 responds to a movement of a charged particle through a homogeneous magnetic
 847 field perpendicular to the particle's momentum and limited to a certain volume.
 848 In general, the shape of such a trajectory with a non-perpendicularly oriented
 849 momentum is a spiral. In our case, the magnetic field is approximately toroidal
 850 and the particle motion is nearly perpendicular to it (verify, could add some
 851 magnetic field plots in different vertical planes; shouldn't have a big effect on the
 852 reconstructed radius anyway). At first, we tested a 2D version of this fit, then
 853 we adapted it to 3D.

854 The field in our detector is not homogeneous, it is therefore not entirely clear
 855 what value of magnetic field should be used along with the fitted radius (using
 856 equations 4.4 and 4.5) to get the best estimate for the kinetic energy. Since we
 857 only use this method as the first iteration of the particle's energy that we later
 858 refine, an optimal solution of this problem is not required. Instead, we tested two
 859 options: taking the value of the field in the middle of the fitted circular arc (or
 860 is it in the middle x of the OFTPC?) and taking the average field along it. We

haven't really tried to plot this for multiple tracks, but these estimates are saved somewhere and could be plotted.

4.2.1 Two-dimensional fit

In the 2D case, the fitted function used for the electron track² described in Section 2.1.1 (one specific track at the time, technically this function doesn't work for a curvature that gets outside of the semicircle) is defined as follows:

$$z(x) = \begin{cases} a_1x + b_1 & x < x_1 \\ z_0 + \sqrt{r^2 - (x - x_0)^2} & x_1 \leq x \leq x_2 \\ a_2x + b_2 & x > x_2 \end{cases}, \quad (4.6)$$

where $a_{1,2}$ and $b_{1,2}$ are the parameters of the lines, (x_0, z_0) is the center of the circle, r is its radius, and $(x_{1,2}, z_{1,2})$ are the coordinates of the function's nodes. That means we have 9 parameters ($z_{1,2}$ are not used in the function) along with 2 continuity conditions and 2 smoothness conditions (9 parameters of the described function, 5 of them independent after taking the conditions into account). For the fit, we use the coordinates of the nodes and the radius of the circle, which gives us 5 independent parameters (only the radius has to be larger than half of the distance between nodes). The continuity conditions (combined with the relations for $z_{1,2}$) are

$$z_{1,2} = a_{1,2}x_{1,2} + b_{1,2} = z_0 - \sqrt{r^2 - (x_{1,2} - x_0)^2}, \quad (4.7)$$

the smoothness conditions are

$$a_{1,2} = \frac{x_0 - x_{1,2}}{\sqrt{r^2 - (x_{1,2} - x_0)^2}}. \quad (4.8)$$

Together with the Equation 4.7 we get the values of $b_{1,2}$

$$b_{1,2} = z_{1,2} - a_{1,2}x_{1,2}. \quad (4.9)$$

For the coordinates of the center of the circle, we can use the fact that the center has to lie on the axis of its chord. In other words, there is a value of a parameter t such that, using the parametric equation of the axis

$$\begin{pmatrix} x_0 \\ z_0 \end{pmatrix} = \begin{pmatrix} \frac{x_1+x_2}{2} \\ \frac{z_1+z_2}{2} \end{pmatrix} + t \begin{pmatrix} \frac{z_2-z_1}{2} \\ \frac{x_1-x_2}{2} \end{pmatrix}. \quad (4.10)$$

At the same time, the center has to be in a distance of r from the nodes:

$$\begin{aligned} (x_1 - x_0)^2 + (z_1 - z_0)^2 &= r^2, \\ \left(\frac{x_1 - x_2}{2} + \frac{z_1 - z_2}{2}t \right)^2 + \left(\frac{z_1 - z_2}{2} + \frac{x_2 - x_1}{2}t \right)^2 &= r^2, \\ \left(\left(\frac{x_2 - x_1}{2} \right)^2 + \left(\frac{z_2 - z_1}{2} \right)^2 \right)t^2 + \left(\frac{x_2 - x_1}{2} \right)^2 + \left(\frac{z_2 - z_1}{2} \right)^2 - r^2 &= 0. \end{aligned} \quad (4.11)$$

²Electron tracks bend towards negative z , we need to use the upper part of the circle

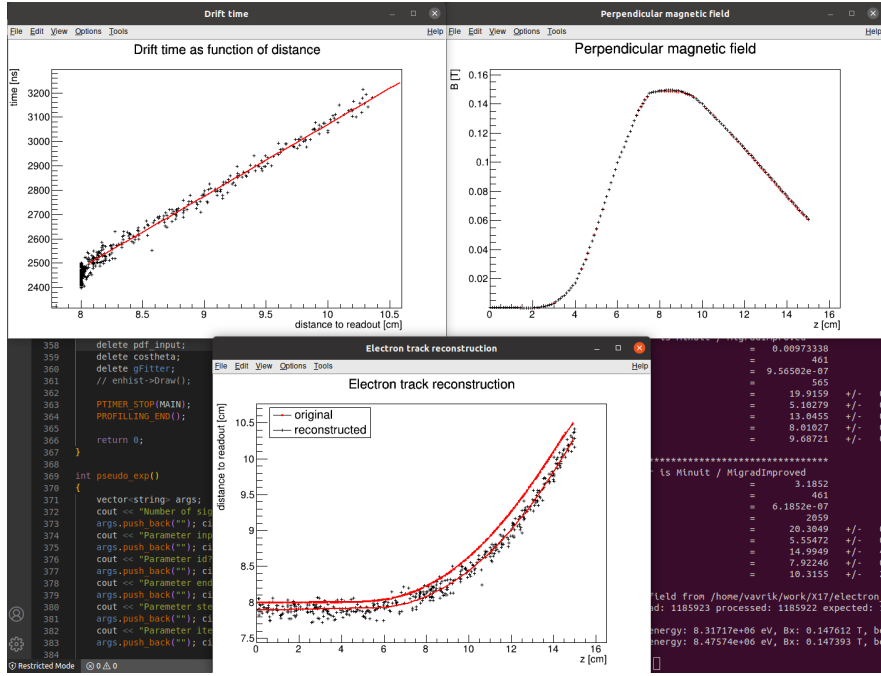


Figure 4.3: First attempt at a track reconstruction using only the drift velocity. Circle and Lines Fit in 2D. Swap for better image, correct coordinates. Bias should be described in the previous chapter, not here.

882 Since our electron track bends towards negative z and $x_2 > x_1$, we only care
883 about the solution with $t > 0$

$$t = \sqrt{\frac{r^2}{\left(\frac{x_2-x_1}{2}\right)^2 + \left(\frac{z_2-z_1}{2}\right)^2} - 1}, \quad (4.12)$$

$$x_0 = \frac{x_1 + x_2}{2} + \frac{z_2 - z_1}{2} \sqrt{\frac{r^2}{\left(\frac{x_2-x_1}{2}\right)^2 + \left(\frac{z_2-z_1}{2}\right)^2} - 1}, \quad (4.13)$$

$$z_0 = \frac{z_1 + z_2}{2} - \frac{x_2 - x_1}{2} \sqrt{\frac{r^2}{\left(\frac{x_2-x_1}{2}\right)^2 + \left(\frac{z_2-z_1}{2}\right)^2} - 1}.$$

884 The function defined in Equation 4.6 along with equations 4.8, 4.9, and 4.13
885 derived using the continuity and smoothness conditions (combined with the re-
886 lations for $z_{1,2}$) fully define our fitted function with parameters $r, x_{1,2}, z_{1,2}$. Some
887 pictures of the fit on the tested track. Results of the fit. Again, the actual fit
888 uses 8-z. Use GeoGebra schematics to generate a picture of 2D geometry.

889 4.2.2 Three-dimensional fit

890 Explain the geometry and least square method used for the 3D fit. Tested on
891 a Runge-Kutta sample, and with microscopic tracks + map simulation.

892 In three dimensions, the shape of a trajectory of a charged particle in a uniform
893 magnetic field is a cylindrical helix. Nevertheless, since we assume that the
894 field is approximately perpendicular to the particle's momentum at all times, we

will further approximate the trajectory with a circular arc (with lines attached smoothly).

We assume that the initial position $\mathbf{X}_0 = (x_0, y_0, z_0)$ and direction θ, φ (spherical angles as in Section 1.3.2) are known, since this information will be provided by TPX3 and MWPC layers. We could further refine it at the end of the current algorithm with some kind of global fit (all detector layers). The fit then has four free parameters (figure):

- the length of the first line l (as measured from the initial position),
- the radius of the circular arc r ,
- the central angle of the arc $\phi_{\max} \in [0, 2\pi]$,
- the direction of the curvature given by the angle $\alpha \in [0, 2\pi]$ (right-handed with respect to the particle direction, $\alpha = 0$ if the particle curves towards negative z in a plane given by $\hat{\mathbf{z}}$ and the direction vector).

Using these parameters, we can derive a parametrization of the whole curve. Let \mathbf{v} be the initial unit direction vector, i.e., using the spherical angles

$$\mathbf{v} = (\cos \varphi \cos \theta, \sin \varphi \cos \theta, \sin \theta)^T, \quad (4.14)$$

then we can parameterize the first line as follows:

$$\mathbf{X}_{L1}(t) = \mathbf{X}_0 + t\mathbf{v} \quad t \in [0, l]. \quad (4.15)$$

This gives us the starting point of the arc

$$\mathbf{X}_1 = \mathbf{X}_{L1}(l) = \mathbf{X}_0 + l\mathbf{v}. \quad (4.16)$$

The vector \mathbf{c}_1 that lies in the plane of curvature and points from \mathbf{X}_1 to the center of curvature can be calculated using a composition of rotations. First, we rotate \mathbf{v} to point in the $\hat{\mathbf{x}}$ direction, the normal for $\alpha = 0$ than points in the $-\hat{\mathbf{z}}$ direction, we apply the α rotation and reverse the rotations into the $\hat{\mathbf{x}}$ direction: (parameters are explained in the bullet points above)

$$\begin{aligned} \mathbf{c}_1 &= R_z(\varphi)R_y(-\theta)R_x(\alpha)R_y\left(\frac{\pi}{2}\right)R_y(\theta)R_z(-\varphi)\mathbf{v}, \\ &= R_z(\varphi)R_y(-\theta)R_x(\alpha)(-\hat{\mathbf{z}}), \\ &= \begin{pmatrix} \cos \varphi & -\sin \varphi & 0 \\ \sin \varphi & \cos \varphi & 0 \\ 0 & 0 & 1 \end{pmatrix} \begin{pmatrix} \cos \theta & 0 & -\sin \theta \\ 0 & 1 & 0 \\ \sin \theta & 0 & \cos \theta \end{pmatrix} \begin{pmatrix} 1 & 0 & 0 \\ 0 & \cos \alpha & -\sin \alpha \\ 0 & \sin \alpha & \cos \alpha \end{pmatrix} \begin{pmatrix} 0 \\ 0 \\ -1 \end{pmatrix}, \quad (4.17) \\ &= \begin{pmatrix} -\sin \alpha \sin \varphi + \cos \alpha \cos \varphi \sin \theta \\ \sin \alpha \cos \varphi + \cos \alpha \sin \varphi \sin \theta \\ -\cos \alpha \cos \theta \end{pmatrix}. \end{aligned}$$

Signs should be correct because right-handed rotation around y rotates z into x and this one is the opposite. Seems like in this part of the code θ is actually taken from the pole. Instead of the equator plane. Similarly by rotating $\hat{\mathbf{y}}$, we can get the normal vector $\mathbf{n} = \mathbf{v} \times \mathbf{c}_1$ perpendicular to the plane of the trajectory:

$$\mathbf{n} = R_z(\varphi)R_y(-\theta)R_x(\alpha)\hat{\mathbf{y}} = \begin{pmatrix} -\cos \alpha \sin \varphi - \sin \alpha \cos \varphi \sin \theta \\ \cos \alpha \cos \varphi - \sin \alpha \sin \varphi \sin \theta \\ \sin \alpha \cos \theta \end{pmatrix}. \quad (4.18)$$

921 This allows us to express the coordinates of the center \mathbf{C} of the circular arc:

$$\mathbf{C} = \mathbf{X}_1 + r\mathbf{c}_1. \quad (4.19)$$

922 We can then get the parametrization and the endpoint of the circular arc using
923 Rodrigues' rotation formula: (all parameters explained in the bullet points above)

$$\begin{aligned} \mathbf{c}_2 &= \mathbf{c}_1 \cos \phi_{\max} + (\mathbf{n} \times \mathbf{c}_1) \sin \phi_{\max} + \mathbf{n}(\mathbf{n} \cdot \mathbf{c}_1)(1 - \cos \phi_{\max}), \\ &= \mathbf{c}_1 \cos \phi_{\max} - \mathbf{v} \sin \phi_{\max}, \end{aligned} \quad (4.20)$$

$$\mathbf{X}_C(\phi) = \mathbf{C} - r(\mathbf{c}_1 \cos \phi - \mathbf{v} \sin \phi) \quad \phi \in [0, \phi_{\max}], \quad (4.21)$$

$$\mathbf{X}_2 = \mathbf{X}_C(\phi_{\max}) = \mathbf{C} - r\mathbf{c}_2, \quad (4.22)$$

924 and if we define the direction vector of the second line, we also get its parametriza-
925 tion

$$\mathbf{w} = \mathbf{v} \cos \phi_{\max} + (\mathbf{n} \times \mathbf{v}) \sin \phi_{\max} = \mathbf{v} \cos \phi_{\max} + \mathbf{c}_1 \sin \phi_{\max}, \quad (4.23)$$

$$\mathbf{X}_{L2}(s) = \mathbf{X}_2 + s\mathbf{w} \quad s \in [0, \infty). \quad (4.24)$$

926 The fit is performed as a (weighted) least square minimization (**MIGRAD**
927 **ROOT**), therefore we need to derive the distance of any point \mathbf{P} to the fitted
928 curve. For the first line, we simply compute the parameter value of the closest
929 point on the line:

$$\begin{aligned} t_P &= \mathbf{v} \cdot (\mathbf{P} - \mathbf{X}_1), \\ d_{P1} &= \|\mathbf{P} - \mathbf{X}_{L1}(t_P)\|. \end{aligned} \quad (4.25)$$

930 If the parameter value is outside of its bounds defined above, we take the bound-
931 ary value instead. The distance to the second line is computed likewise. For
932 the circular arc (specific circular arc in the fit), we find the closest point (on the
933 arc) by projecting the center connecting line onto the arc plane:

$$\mathbf{X}_{PC} = \mathbf{X}_C + r \frac{(\mathbf{P} - \mathbf{X}_C) - (\mathbf{n} \cdot (\mathbf{P} - \mathbf{X}_C))\mathbf{n}}{\|(\mathbf{P} - \mathbf{X}_C) - (\mathbf{n} \cdot (\mathbf{P} - \mathbf{X}_C))\mathbf{n}\|}, \quad (4.26)$$

$$d_{PC} = \|\mathbf{P} - \mathbf{X}_{PC}\| \quad (4.27)$$

934 Potential problem in the implementation – might not be correctly handling ϕ
935 out of bounds, the distance could be sometimes underestimated because of this.

936 The shortest distance out of d_{P1}, d_{PC}, d_{P2} is then taken as the distance to the curve.■

937 When calculating energy with the average field, only the arc is considered. Mid-
938 dle field in the current implementation taken in the middle x plane (intersection
939 with the curve). TVirtualFitter+MIGRAD, maximal num of iterations, tolera-
940 tion. Different uncertainties in x, y, z not taken into account.

941 Fit details (parameter bounds, initial setting).

942 4.2.3 Testing on a Runge-Kutta sample

943 The three dimensional circle and lines fit was tested on a sample of Runge-Kutta
944 tracks with randomized parameters described in Section 2.2.1. These tracks of
945 primary electrons and positrons consist of points calculated with the RK4 algo-
946 rithm for a given proper time step (step can be adjusted by dividing by the gamma
947 factor → detector time). Fitting with circle only was also partially implemented
948 (didn't work but could be fixed/tuned).

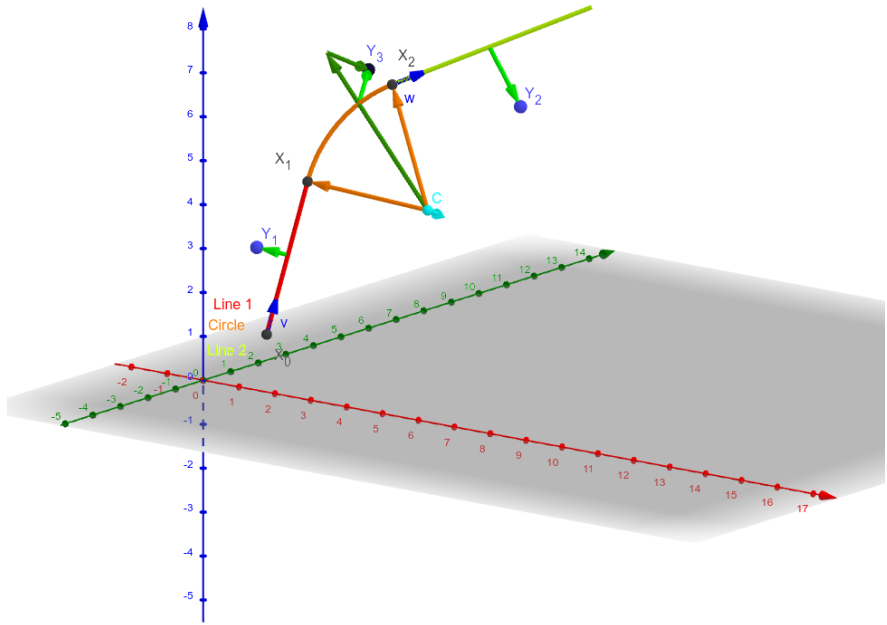


Figure 4.4: Circle and Lines Fit 3D geometry. Swap for better image.

949 4.3 Runge-Kutta Fit

950 The Runge-Kutta fit uses the Runge-Kutta 4th order (RK4) numerical integration
 951 of the equation of motion (see Section 2.2) to find the best values of the track
 952 parameters – the track origin, initial velocity direction and the kinetic energy. In
 953 order to speed up the energy reconstruction, an initial guess of these parameters
 954 can be obtained from the 3D circle fit described in the previous section. Fur-
 955 thermore, assuming we know the track origin and orientation, we can perform
 956 a single parameter fit of the kinetic energy (**do some profiling and show that it is**
 957 **faster – below in the microscopic testing**).

958 The fit is performed as a least square minimization of the (weighted) distances
 959 of the track points (true ionization vertices from the simulation or reconstructed
 960 points). The simulated RK4 track consists of line segments with known endpoints,
 961 therefore we can calculate the distance of a point from this segment analogically
 962 to Equation 4.25 with \mathbf{v} given as a unit vector in the direction of the segment.

963 We need to find the segment with the lowest distance. We assume, that
 964 the distance $d_{\mathbf{P}}(\tau)$ of a point \mathbf{P} to the point on the track $\mathbf{X}(\tau)$ has a single
 965 minimum (local and global), no local maximum (except the interval endpoints)
 966 and no saddle point

$$\exists! \tau_{\min} \in [0, \tau_N]: (\forall \tau \in [0, \tau_N]: d_{\mathbf{P}}(\tau) \geq d_{\mathbf{P}}(\tau_{\min})) \vee \frac{dd_{\mathbf{P}}}{d\tau}(\tau_{\min}) = 0, \quad (4.28)$$

967 where N is the number of RK4 steps. This is a reasonable assumption for a track
 968 with an approximate shape of a circular arc with a radius r , since the distance d
 969 from a point \mathbf{C} on the corresponding circle of a point \mathbf{P} offset by a from the arc
 970 plane and by b from the arc's center when projected on its plane is given by the

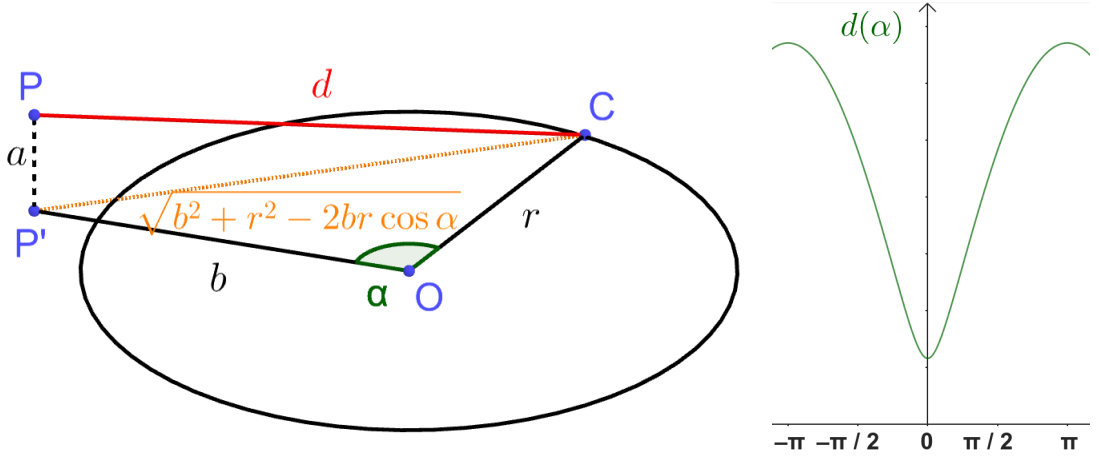


Figure 4.5: Demonstration of the convexity of the distance function $d(\alpha)$ for a circular track (see Equation 4.29).

971 law of cosines:

$$d^2 = a^2 + b^2 + r^2 - 2br \cos \alpha, \quad (4.29)$$

972 where α is the angle between points \mathbf{C} and \mathbf{P} as seen from the center of the arc
973 (see Figure 4.5). This function is strictly convex for $\alpha \in \left(-\frac{\pi}{2}, \frac{\pi}{2}\right)$ and in our case,
974 the center of the arc lies outside of the detector and α is restricted to a small
975 interval around zero (especially considering that the initial guess should make the
976 fitted trajectory reasonably close to any relevant point, in the worst-case scenario,
977 the distance is overestimated which should keep the fit from converging to such
978 solutions).

979 In a more general case, if we consider the vector $\mathbf{a}(\tau) = \mathbf{P} - \mathbf{X}(\tau)$ whose size
980 is $\|\mathbf{a}(\tau)\| = d_{\mathbf{P}}(\tau)$, then the we get

$$2d_{\mathbf{P}} \frac{dd_{\mathbf{P}}}{d\tau} = \frac{dd_{\mathbf{P}}^2}{d\tau} = \frac{d}{d\tau} \sum_i a_i^2 = 2 \sum_i a_i \frac{da_i}{d\tau} = 2\mathbf{a} \cdot \frac{d\mathbf{a}}{d\tau} = -2\mathbf{a} \cdot \frac{d\mathbf{X}}{d\tau}, \quad (4.30)$$

981 therefore for the derivative of $d_{\mathbf{P}}(\tau)$ to be zero, $\mathbf{a}(\tau)$ has to be perpendicular
982 to the tangent of the track. In 3D, for a given $\mathbf{X}(\tau)$, this condition restricts \mathbf{P}
983 to a plane. This means that for a curving track we can find a point \mathbf{P} for any
984 two points $\mathbf{X}(\tau), \mathbf{X}(\sigma)$ with non-parallel tangents that has $\frac{dd_{\mathbf{P}}}{d\tau}(\tau) = \frac{dd_{\mathbf{P}}}{d\tau}(\sigma) =$
985 $= 0$, which violates the assumption 4.28. If we have a circle-and-lines track as
986 described in the previous sections, such a point has to lie outside of the circular
987 sector given by the arc.

988 For a planar track, the envelope of all its normals is the evolute of the curve
989 (i.e., the set of centers of all its osculating circles). If the track has a monotonous
990 tangent angle

$$\alpha(\tau) = \text{atan} \frac{\frac{dX_2}{d\tau}}{\frac{dX_1}{d\tau}} \quad (4.31)$$

991 with minimal and maximal α differing by less than π (i.e., the track changes
992 direction by less than 180°), then all intersections of the track's normals must lie
993 on the side of the evolute closer to the track (not obvious?, sometimes the sides
994 are opposite?). At the same time, the intersection must lie in the half planes
995 given by the normals at the beginning and the end of the curve and pointing

996 away from the curve. Together, these three boundaries define a closed shape that
997 will lie outside of the OFTPC for a typical track in our detector.

998 With the assumption 4.28, we can find the segment on the RK4 track with
999 the lowest distance to a given point \mathbf{P} using a binary search algorithm. Let
1000 the distance of the point from the n -th vertex be $d_{\mathbf{P},n}$. Then the difference
1001 $\Delta d_{\mathbf{P},n} = d_{\mathbf{P},n} - d_{\mathbf{P},n-1}$ satisfies

$$\begin{aligned}\Delta d_{\mathbf{P},n} &< 0 \quad \forall n \text{ such that } \tau_n < \tau_{\min}, \\ \Delta d_{\mathbf{P},n} &> 0 \quad \forall n \text{ such that } \tau_{n-1} > \tau_{\min}.\end{aligned}\tag{4.32}$$

1002 Therefore, we can search for the segment containing $d_{\mathbf{P},\min}$ with binary search
1003 starting with $\Delta d_{\mathbf{P},1}$ and $\Delta d_{\mathbf{P},N}$, then calculate the difference $\Delta d_{\mathbf{P},m}$ for the middle
1004 index $m = \left\lfloor \frac{N+1}{2} \right\rfloor$. If $\Delta d_{\mathbf{P},m} > 0$ (minor bug in the implementation – if the value
1005 for the maximal index is negative, it shouldn't change anything), we can replace
1006 the higher index with m , otherwise we replace the lower index. The search stops
1007 when the difference between the minimal and maximal index is one. Would
1008 it be better if they were the same (maybe not)? Then the minimal value is
1009 $d_{\mathbf{P},n-1}$ or $d_{\mathbf{P},N}$ and we can take the minimum of the distances from the two
1010 segments connected to $n-1$. Currently taking the maximal index (and starting
1011 at $N-2$ maximal index $\leftrightarrow N-1$ -th point), this should be equivalent, since either
1012 $\Delta d_{\mathbf{P},\max} > 0$ (in the code is equivalent to max-1 here) or we are at $N-1$. The
1013 minimum of the two distances still taken.

1014 Same details with MIGRAD etc. as previously.

1015 4.3.1 Testing on a microscopic sample

1016 The Runge-Kutta fit together with the 3D circle-and-lines pre-fit was tested
1017 on a sample of tracks simulated using the microscopic simulation described in
1018 Section 2.1. At first, few tracks with randomized initial parameters (same as
1019 the Runge-Kutta sample in Section 2.2.1) were generated for preliminary testing.
1020 Later, a sample with a grid-like distribution of track parameters was generated
1021 (see Section 2.1.2 for details).

1022 Initial parameters of the HEED track (also should be in the first testing track
1023 → subsection of microsim?). Initial parameters set in the circle fit (if electron set
1024 alpha one way, otherwise other way) and parameter bounds.

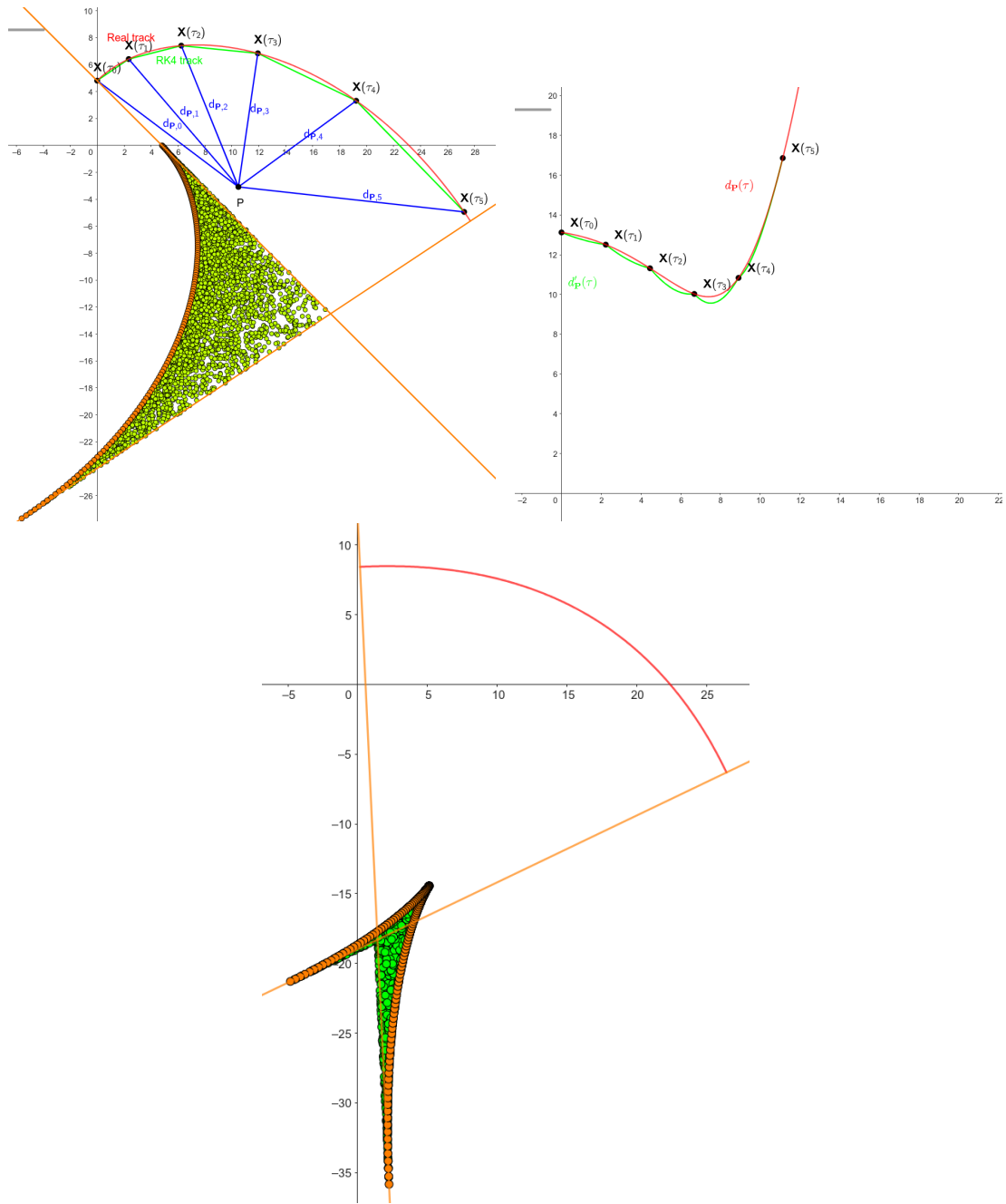


Figure 4.6: some provisional figures

1025 Conclusion

1026 Here or at the end of each section. Something about the future of this work?

1027 Notes

1028 General notes about the thesis:

- 1029 • Check that all of the classes and other code are marked the same way in
1030 the text. I used italics somewhere, could use different font for this instead.
- 1031 • Check unbreakable space in front of articles. Remove excessive article usage
1032 with proper nouns.
- 1033 • Currently using margins for single-sided printing (bigger on the left side).
- 1034 • Check that present tense is used
- 1035 • Active vs passive voice usage
- 1036 • American English quotation marks (") instead of British English (').
- 1037 • Some of the overfull hbox warnings might change if duplex printing is used
1038 (they generate black rectangles on the edge of the page), leaving them be
1039 for now
- 1040 • Check nobreakdash usage (is it always necessary)
- 1041 • Check capitalized references (e.g., Figure, Section, Equation)
- 1042 • Check \(...\mathbf{\}) math mode instead of \\$...\$. (actually unlike \[...\] math mode,
1043 there is apparently no real benefit to this clumsy syntax)
- 1044 • Use siunitx package to ensure correct formatting, physics package for deriva-
1045 tives.
- 1046 • Check other stuff that's written in the MFF UK template. Apparently it
1047 has since been updated and there are some differences (check for them).
- 1048 • Check correct subscripts in equation (italics vs no italics)
- 1049 • Consistent bold marking of points/vectors
- 1050 • Correct footnotes (capital letters, etc.).
- 1051 • Might have to mention GeoGebra as per the non-commercial license agree-
1052 ment (Made with GeoGebra®) – maybe put it into acknowledgments next
1053 to the MetaCentrum credit? And list all of the figures where GeoGebra was
1054 used?
- 1055 • Maybe make some section outside of References specifically for literature?
1056 (such as the old CERN TPC review, ATOMKI review is currently not
1057 mentioned, not sure if some Wikipedia articles should get a mention or how
1058 do these things work)
- 1059 • Consistent use of `bm` vs `mathbf`

- Consistent use of $\bar{\mathcal{M}}$ instead of \mathcal{M} when talking about the map of the means (so most of the time)
- Proper equation numbering when deriving a relation
- Hugo should be mentioned somewhere in the title probably?
- Consistent itemize/enumerate style (namely spacing) that looks good (ideally set by some macro? maybe the new MFF UK template will solve this?)
- Consistent gas mixture notation (e.g. 90:10 Ar:CO₂).

1067 Random notes:

- Terminology consistency – ionization/primary/secondary electrons
- Consistent TPC vs OFTPC acronym usage in the text or individual chapters.
- Only electrons that start and end in the sector closer than 0.5 cm are used for reconstruction (newest version).
- Attachment, Penning transfer and secondary ionization not considered in the microscopic simulation.
- Suspicious artifacts of trilinear interpolation in Figure 1.7. **Fixed – integers instead of doubles in the implementation, influenced reconstruction SIGNIFICANTLY (but not simulation).**
- Profiling of the reconstruction!!!! Find out what's taking the most time (probably Runge-Kutta integration which the fit calls a lot). Could gradually decrease the step size to refine the fit instead of making it small right away (arbitrarily small – the effect of this was never tested). This could take some time to do properly (find a profiler or make profiling macros).
- Slow drift velocity good for z reconstruction, too low leads to recombination
- Could add link to the GitHub repository, mention CMake? Details about simulating on MetaCentrum?
- The first used track had 8 MeV momentum $p = \gamma mv$ (not kinetic energy $E_{\text{kin}} = (\gamma - 1)mc^2 = \sqrt{p^2c^2 + m^2c^4} - mc^2 \approx 7.5$ MeV)
- Maybe cite Garfield++ user manual instead? Using TRandom3 for random number generation.
- Does the RK fit error correlate with the actual error?

1091 Future

1092 Things planned for the future:

- Testing the reconstruction algorithm by measuring real particles with a known energy distribution.
- The **Fast Simulation with Ionization Electron Map** is planned for the future. It will use the HEED program [30] to simulate the primary particle and the Ionization Electron Map (see Section 3.2) to simulate the drift

1098 of secondary electrons. It should be significantly faster than the Microscopic
1099 Simulation but offer comparable precision since it will rely on an already
1100 simulated drift map. (Primary track simulated in HEED. Readout parameters
1101 by interpolating the map. Diffusion from the map for randomization.)

- 1102 • Account for GEM, delta electrons, ...
- 1103 • Likelihood approach instead of least squares (if it improves the reconstruction
1104 significantly), we should at least use a better method than taking
1105 the center of the TPC bin.
- 1106 • More detailed electric field simulation (if needed, GEM will have more com-
1107 plex field, some irregularities in the field should be considered)
- 1108 • Account for the triggering in MWPC/TPX3 (particle travels from TPX3
1109 to MWPC basically immediately – fraction of a nanosecond so there should
1110 be no significant difference)

1111 Likelihood - inverse map

1112 If we wanted to further improve this procedure, taking into account the whole
1113 map \mathcal{M} , we could make an "inverse map" from \mathcal{R} to distributions on \mathcal{D} . We could
1114 achieve this by taking the normalized probability density of an electron with initial
1115 coordinates (x, y, z) having readout coordinates (x', y', t) . If we fix (x', y', t) , we
1116 get an unnormalized probability density $f(x, y, z) = \mathcal{M}_{(x,y,z)}(x', y', t)$ (assuming
1117 that all initial coordinates are a priori equally likely). This could potentially
1118 improve the discrete reconstruction if we take the mean value of this probability
1119 density across the pad and time bin

$$f_{\text{pad, bin}}(x, y, z) = \frac{1}{A_{\text{pad}} \Delta t_{\text{bin}}} \int_{\text{pad, bin}} \mathcal{M}_{(x,y,z)}(x', y', t) dx' dy' dt \quad (4.33)$$

1120 and using it for a likelihood fit instead of using least squares. This still assumes
1121 that all initial coordinates are equally likely which is clearly not the case for
1122 a primary particle track. In the future, we could even use the fast track simulation
1123 with the map (should be possible to make around 1000 tracks per minute per core
1124 with current settings), create a big set of tracks with reasonable parameters and
1125 use these to get an approximation of the probability distribution of the detector
1126 response. Some approximations would be necessary when interpreting the data to
1127 decrease the degrees of freedom of this distribution (we would have to pick a set of
1128 parameters and assume that some of them are independent). This could give us
1129 an idea about the best achievable resolution (how significantly will the detector
1130 response differ for a given change in energy). If the difference is significant, we
1131 could try to further improve the likelihood fit.

Bibliography

1. *Garfield++* [<https://garfieldpp.web.cern.ch/garfieldpp/>]. [N.d.]. Accessed: 2023-05-18.
2. BRUN, Rene; RADEMAKERS, Fons. Root — An Object Oriented Data Analysis Framework. *Nucl. Instrum. Methods Phys. Res. Sect. A: Accel. Spectrom. Detect. Assoc. Equip.* 1997, vol. 389, no. 1–2, pp. 81–86. Available from DOI: 10.1016/s0168-9002(97)00048-x. Proceedings AIHENP'96 Workshop, Lausanne, Sep. 1996, See also <https://root.cern/>, Paper published in the Linux Journal, Issue 51, July 1998.
3. *About MetaCentrum* [<https://metavo.metacentrum.cz/en/about/index.html>]. 2023. Accessed: 2024-11-27.
4. ROSE, M. E. Internal Pair Formation. *Phys. Rev.* 1949, vol. 76, pp. 678–681. Available from DOI: 10.1103/PhysRev.76.678.
5. ESSIG, R. et al. *Dark Sectors and New, Light, Weakly-Coupled Particles*. 2013. Available from arXiv: 1311.0029 [hep-ph].
6. DE BOER, F.W.N. et al. A deviation in internal pair conversion. *Phys. Lett. B*. 1996, vol. 388, no. 2, pp. 235–240. ISSN 0370-2693. Available from DOI: [https://doi.org/10.1016/S0370-2693\(96\)01311-1](https://doi.org/10.1016/S0370-2693(96)01311-1).
7. BOER, F W N de et al. Excess in nuclear pairs near 9 MeV/ invariant mass. *J. Phys. G: Nucl. Part. Phys.* 1997, vol. 23, no. 11, p. L85. Available from DOI: 10.1088/0954-3899/23/11/001.
8. BOER, F W N de et al. Further search for a neutral boson with a mass around 9 MeV/c². *J. Phys. G: Nucl. Part. Phys.* 2001, vol. 27, no. 4, p. L29. Available from DOI: 10.1088/0954-3899/27/4/102.
9. VITÉZ, Attila et al. Anomalous Internal Pair Creation in ⁸Be as a Signature of the Decay of a New Particle. *Acta Phys. Pol. B - ACTA PHYS POL B*. 2008, vol. 39, p. 483.
10. KRASZNAHORKAY, A. et al. Searching for a light neutral axial-vector boson in isoscalar nuclear transitions. *Frascati Phys. Ser.* 2012, vol. 56, p. 86.
11. KRASZNAHORKAY, A. J. et al. Observation of Anomalous Internal Pair Creation in ⁸Be: A Possible Indication of a Light, Neutral Boson. *Phys. Rev. Lett.* 2016, vol. 116, no. 4. ISSN 1079-7114. Available from DOI: 10.1103/physrevlett.116.042501.
12. TILLEY, D.R. et al. Energy levels of light nuclei A=8,9,10. *Nucl. Phys. A*. 2004, vol. 745, no. 3, pp. 155–362. ISSN 0375-9474. Available from DOI: <https://doi.org/10.1016/j.nuclphysa.2004.09.059>.
13. SAS, N. J. et al. *Observation of the X17 anomaly in the ⁷Li(p,e⁺e⁻)⁸Be direct proton-capture reaction*. 2022. Available from arXiv: 2205.07744 [nucl-ex].
14. KRASZNAHORKAY, A. J. et al. New anomaly observed in ⁴He supports the existence of the hypothetical X17 particle. *Phys. Rev. C*. 2021, vol. 104, no. 4. ISSN 2469-9993. Available from DOI: 10.1103/physrevc.104.044003.

- 1174 15. TILLEY, D.R. et al. Energy levels of light nuclei A = 4. *Nucl. Phys. A*.
 1175 1992, vol. 541, no. 1, pp. 1–104. ISSN 0375-9474. Available from DOI: [https://doi.org/10.1016/0375-9474\(92\)90635-W](https://doi.org/10.1016/0375-9474(92)90635-W).
- 1177 16. KRASZNAHORKAY, A. J. et al. New anomaly observed in ^{12}C supports the
 1178 existence and the vector character of the hypothetical X17 boson. *Phys. Rev.*
 1179 *C*. 2022, vol. 106, p. L061601. Available from DOI: 10.1103/PhysRevC.106.
 1180 L061601.
- 1181 17. AJZENBERG-SELOVE, F. Energy levels of light nuclei A = 11,12. *Nucl. Phys.*
 1182 *A*. 1990, vol. 506, no. 1, pp. 1–158. ISSN 0375-9474. Available from DOI:
 1183 [https://doi.org/10.1016/0375-9474\(90\)90271-M](https://doi.org/10.1016/0375-9474(90)90271-M).
- 1184 18. KÁLMÁN, Péter; KESZTHELYI, Tamás. Anomalous internal pair creation.
 1185 *The Eur. Phys. J. A*. 2020, vol. 56. Available from DOI: 10.1140/epja/
 1186 s10050-020-00202-z.
- 1187 19. ALEKSEJEVS, A. et al. *A Standard Model Explanation for the "ATOMKI*
 1188 *Anomaly*". 2021. Available from arXiv: 2102.01127 [hep-ph].
- 1189 20. FENG, Jonathan L. et al. Protophobic Fifth-Force Interpretation of the Ob-
 1190 served Anomaly in ^8Be Nuclear Transitions. *Phys. Rev. Lett.* 2016, vol. 117,
 1191 p. 071803. Available from DOI: 10.1103/PhysRevLett.117.071803.
- 1192 21. ANH, Tran The et al. Checking the 8Be Anomaly with a Two-Arm Electron
 1193 Positron Pair Spectrometer. *Universe*. 2024, vol. 10, no. 4, p. 168. ISSN 2218-
 1194 1997. Available from DOI: 10.3390/universe10040168.
- 1195 22. ABRAAMYAN, Kh. U. et al. *Observation of structures at ~ 17 and ~ 38*
 1196 *MeV/c 2 in the $\gamma\gamma$ invariant mass spectra in pC, dC, and dCu collisions at*
 1197 *p_{lab} of a few GeV/c per nucleon*. 2023. Available from arXiv: 2311.18632
 1198 [hep-ex].
- 1199 23. THE MEG II COLLABORATION et al. *Search for the X17 particle in $^7\text{Li}(p, e^+e^-)^8\text{Be}$*
 1200 *processes with the MEG II detector*. 2024. Available from arXiv: 2411.07994
 1201 [nucl-ex].
- 1202 24. ABED ABUD, Adam et al. A Gaseous Argon-Based Near Detector to En-
 1203 hance the Physics Capabilities of DUNE. 2022. Available from DOI: 10.
 1204 48550/arXiv.2203.06281.
- 1205 25. LOKEN, Stewart C. et al. Performance of the Signal Processing System for
 1206 the Time Projection Chamber. *IEEE Trans. on Nucl. Sci.* 1983, vol. 30, no.
 1207 1, pp. 162–166. Available from DOI: 10.1109/TNS.1983.4332243.
- 1208 26. HILDÉN, T. et al. Optical quality assurance of GEM foils. *Nucl. Instrum.*
 1209 *Methods Phys. Res. Sect. A: Accel. Spectrom. Detect. Assoc. Equip.* 2015,
 1210 vol. 770, pp. 113–122. ISSN 0168-9002. Available from DOI: 10.1016/j.j.
 1211 nima.2014.10.015.
- 1212 27. AHMED, Misbah Uddin. *Simulation of the electron and ion movement through*
 1213 *a 4-GEM stack*. 2021. Institut für Kernphysik.
- 1214 28. MARMELAD. *3D interpolation2.svg*. 2025. Available also from: https://commons.wikimedia.org/wiki/File:3D_interpolation2.svg. Licensed
 1215 under CC BY-SA 3.0 (<https://creativecommons.org/licenses/by-sa/3.0/legalcode>). Accessed: 9-April-2025.

- 1218 29. CMGLEE. *Trilinear interpolation visualisation*. 2025. Available also from:
1219 [https://commons.wikimedia.org/wiki/File:Trilinear_interpolation_](https://commons.wikimedia.org/wiki/File:Trilinear_interpolation_visualisation.svg)
1220 [visualisation.svg](https://creativecommons.org/licenses/by-sa/3.0/legalcode). Licensed under CC BY-SA 3.0 (<https://creativecommons.org/licenses/by-sa/3.0/legalcode>). Accessed: 26-March-2025.
1221
- 1222 30. SMIRNOV, I.B. Modeling of ionization produced by fast charged particles in
1223 gases. *Nucl. Instrum. Methods Phys. Res. Sect. A: Accel. Spectrom. Detect.*
1224 *Assoc. Equip.* 2005, vol. 554, no. 1, pp. 474–493. ISSN 0168-9002. Available
1225 from DOI: <https://doi.org/10.1016/j.nima.2005.08.064>.

1226 **Acknowledgments:** Computational resources were provided by the e-INFRA
1227 CZ project (ID:90254), supported by the Ministry of Education, Youth and Sports
1228 of the Czech Republic. **Figures that were drawn with GeoGebra.**

1229 List of Figures

1230	0.1	The ATOMKI anomalous IPC measured for different nuclei.	5
1231	0.2	Results from the Hanoi spectrometer – angular e^+e^- pair correlations measured in the ${}^7\text{Li}(p, e^+e^-){}^8\text{Be}$ reaction at $E_p = 1225$ keV [21].	6
1232	0.3	Results from the MEG II experiments – angular correlation of e^+e^- pairs with $E_{\text{sum}} \in [16, 20]$ MeV measured in the ${}^7\text{Li}(p, e^+e^-){}^8\text{Be}$ reaction with proton beam energies 500 and 1080 keV. The 500 keV dataset is fitted with Monte Carlo of both the IPC deexcitation and the EPC produced by gammas [23].	7
1233	0.4	Schematics of the detector at the Van der Graaff facility at IEAP CTU.	7
1234	1.1	Particle identification in the PEP-4 TPC at SLAC based on the energy loss per distance $\frac{dE}{dx}$ [24].	9
1235	1.2	Schematic view of the PEP-4 TPC [25]. A charged particle produced in a collision in the beam pipe creates a spiral ionization track in the magnetic field. The central cathode then accelerates ionization electrons towards the endcap anode wires where they are multiplied and read out.	10
1236	1.3	A scanning electron microscope image of a GEM foil [26].	12
1237	1.4	Garfield simulation of an avalanche in a GEM hole [27]. An incoming electron (orange) is accelerated in the strong electric field of the GEM and causes further ionization multiplying the number of free electrons (orange). Most of the produced cations (red) are captured by the GEM cathode.	13
1238	1.5	Schematics of the first sector OFTPC with detector space coordinates.	15
1239	1.6	Pad layout of the OFTPC and its parameters. Pads 102, 124 and 127 are irregular, the rest has the same dimensions.	16
1240	1.7	Magnetic field simulation results. The OFTPC volume and the vacuum tube are marked with black lines, the magnets are marked with red lines. The coordinates of the magnets from the CAD drawing seem to be 9/10 of the ones from the magnetic simulation (confirm and fix).	17
1241	1.8	Visualization of trilinear interpolation as a composition of linear interpolations (inspired by [28]). We want to interpolate the value in the red point C. First we interpolate between the four pairs of blue points sharing the last two indices along the x -axis (Eq. 1.14), then between the two pairs of the resulting green points along the y -axis (Eq. 1.15) and finally between the two resulting orange points along the z -axis to get the final red value (Eq. 1.16).	18
1242	1.9	Geometric interpretation of trilinear interpolation as expressed in Equation 1.18. The colored dots represent the values in given points and the colored boxes represent the volume in the opposite corner by which the corresponding values are multiplied. The black dot represents the interpolated value which is multiplied by the entire volume [29].	18

1274	2.1 Comparison of drift lines for two different gas mixtures 90:10 and 1275 70:30 Ar:CO ₂ . The electron track is marked in black, the drift lines 1276 of the ionization electrons are marked in orange. In this example, 1277 we assume a larger OFTPC volume with readout at $z = 8$ cm.	21
1278	2.2 A visualization of a set of tracks from the grid-like testing sample 1279 with the same kinetic energy.	22
1280	2.3 A comparison of the HEED track from the microscopic simulation 1281 in Section 2.1.1 with a Runge-Kutta track with the same initial 1282 parameters and $\tau_{\text{step}} = 0.1$ ps (reducing the step further doesn't 1283 make a visible difference). In the view of the tracks on the left, 1284 the distance of the HEED ionization electrons from the RK4 track 1285 is exaggerated 1000 \times . On the right, the dependence of the HEED 1286 electrons residuals (i.e., their shortest distance to the RK4 track) 1287 on their z -coordinate is shown. The images look the same even for 1288 100,000x smaller step, so the residuals are a result of something 1289 that HEED does.	24
1290	3.1 Dependence of the drift time on the z coordinate in 90 % argon 1291 and 10 % CO ₂ atmosphere, fitted with a linear function. The fitted 1292 function gives us the average drift velocity in the gas and can be 1293 used for rough reconstruction in our TPC. Swap for better image 1294 with axis labels, etc. Maybe write the fitted equation.	26
1295	3.2 The first attempt of a track reconstruction using only the drift 1296 velocity. This approach works well in a standard TPC (ideally cite 1297 some source). 90 % argon and 10 % CO ₂ atmosphere. Swap for 1298 better image, correct coordinates.	27
1299	3.3 First attempt at a track reconstruction using only the drift veloc- 1300 ity, residues. Swap for better image, correct coordinates. What's 1301 causing the shift? Explain details.	27
1302	3.4 Example of map generation. Swap for better image, correct coor- 1303 dinates.	30
1304	3.5 Example reconstruction with the map. Swap for better image, 1305 correct coordinates.	30
1306	3.6 Selection of the points for interpolation. Create better images; use 1307 the explanation interpolation vs. extrapolation strange property. 1308 Solution 2 probably does not make much sense.	33
1309	4.1 Example of a fitted reconstructed track. Swap for better image. .	35
1310	4.2 First attempt at a track reconstruction using only the drift velocity. 1311 Spline energy reconstruction attempt. Swap for better image(s) – 1312 subfigure environment, correct coordinates.	37
1313	4.3 First attempt at a track reconstruction using only the drift veloc- 1314 ity. Circle and Lines Fit in 2D. Swap for better image, correct 1315 coordinates. Bias should be described in the previous chapter, not 1316 here.	39
1317	4.4 Circle and Lines Fit 3D geometry. Swap for better image.	42
1318	4.5 Demonstration of the convexity of the distance function $d(\alpha)$ for 1319 a circular track (see Equation 4.29).	43
1320	4.6 some provisional figures	45

₁₃₂₁ **List of Tables**

¹³²² List of Abbreviations

¹³²³ **GEM** Gas Electron Multiplier

¹³²⁴ **HEED** High Energy Electro-Dynamics

¹³²⁵ **IEAP CTU** Institute of Experimental and Applied Physics, Czech Technical
¹³²⁶ University in Prague

¹³²⁷ **IPC** Internal Pair Creation

¹³²⁸ **EPC** External Pair Creation

¹³²⁹ **Micromegas** MICRO-MEsh GAseous Structure

¹³³⁰ **MWPC** Multi-Wire Proportional Chamber

¹³³¹ **OFTPC** Orthogonal Fields TPC

¹³³² **RK4** Runge-Kutta 4th order

¹³³³ **TPC** Time Projection Chamber

¹³³⁴ **ToA** time-of-arrival

¹³³⁵ **ToT** time-over-threshold

¹³³⁶ **TPX3** Timepix 3